Addressing Complex Transition Metal Oxides at the Nanoscale: Bottom-Up Syntheses of Nano-objects and Properties

David Portehault, Francisco Gonell, Isabel Gómez-Recio

To cite this version:

David Portehault, Francisco Gonell, Isabel Gómez-Recio. Addressing Complex Transition Metal Oxides at the Nanoscale: Bottom-Up Syntheses of Nano-objects and Properties. Tailored Functional Oxide Nanomaterials: From Design to Multi-Purpose Applications, 1, Wiley, 2022, ⟨10.1002/9783527826940.ch2⟩. ⟨hal-03813202⟩

HAL Id: hal-03813202

https://hal.science/hal-03813202v1

Submitted on 29 Oct 2022

Addressing complex transition metal oxides at the nanoscale: bottom-up syntheses of nano-objects and properties

David Portehault,* Francisco Gonell, Isabel Gómez-Recio

[a] Sorbonne Université, CNRS, Laboratoire de Chimie de la Matière Condensée de Paris (CMCP), 4 place Jussieu, F-75005, Paris, France

Corresponding author: david.portehault@sorbonne-universite.fr

Keywords: perovskites, layered oxides, Magneli phases, metastable oxides, electrocatalysts, nanocrystals, colloidal synthesis, liquid-phase synthesis, molten salts, sol-gel

ABSTRACT:

An impressive library of functional oxide nanomaterials is now available, encompassing multicompartment nanoparticles and heterostructures in general that enable further tuning of the properties. Nonetheless, the vast majority of these nano-objects is built on relatively common oxides, easily synthesized at the nanoscale by chemical methods known since decades. This range of nanoscaled oxides is narrow compared to the library of bulk oxides. Extending the portfolio of oxide compositions at the nanoscale is mandatory to strengthen research efforts on the role of the nanoscale on the properties, and on the emergence of new properties. This chapter provides an overview of the synthesis techniques developed since few years to address complex oxide nanomaterials, encompassing multicationic oxides, oxides of metals with uncommon oxidation states, and new oxide crystal structures accessible only at the nanoscale. For each case, we illustrate the relevance of targeting such complex oxides by discussing their specific properties.

Dr. David Portehault obtained his PhD in chemistry of materials at University Pierre and Marie Curie in 2008. He then became a senior postdoctoral fellow at the Max Planck Institute for Colloids and Interfaces until 2010. Since then, he is researcher of the French National Centre for Scientific Research (CNRS) at the Laboratory of Condensed Matter of Paris (LCMCP) hosted by Sorbonne University. His main research topic is the exploration of new synthesis pathways at the edge of solid-state chemistry and solution chemistry to discover original nanomaterials, including metal oxides, borides, silicides and carbides for energy-related properties, focused on electrocatalysis. Among his most significant distinctions, he received the EuChemS Lecture Award in 2019 and was granted with an European Research Council Consolidator Grant also in 2019.

Dr. Francisco Gonell obtained his B.Sc degree in chemistry from Universitat Jaume I (Caselló, Spain) where he also obtained his PhD (2017) under the guidance of Dr. Beatriz Julián-López and Prof. Avelino Corma working in the synthesis of multifunctional nanomaterials and the study of their acid-base/redox catalytic, photocatalytic and luminescence properties. In 2017, he moved to “Laboratorie de Chimie de la Matière Condensée de Paris” (France) to work with Dr. David Portehault and Prof. Clément Sanchez on the synthesis of multicationic oxides nanomaterials in molten salts and the study of their electrocatalytic and magnetic properties. In 2020 he incorporated at “Instituto de Tecnología Química” (ITQ, València, Spain) as a postdoctoral researcher. His main interest is the synthesis design of multifunctional nanomaterials for their application in electrocatalysis.

Dr. Isabel Gómez-Recio is a postdoctoral fellow of the French National Centre for Scientific Research (CNRS), researcher at the Laboratory Chimie de la Matière Condensée de Paris (LCMCP) at Sorbonne University. She got her Chemistry PhD degree at University Complutense of Madrid (UCM) in 2018. Her research covers topics as solid-state chemistry, electron microscopy as well as synthesis and characterization of nanoparticles with the aim of understanding their formation and afterwards of developing materials with tuned properties.

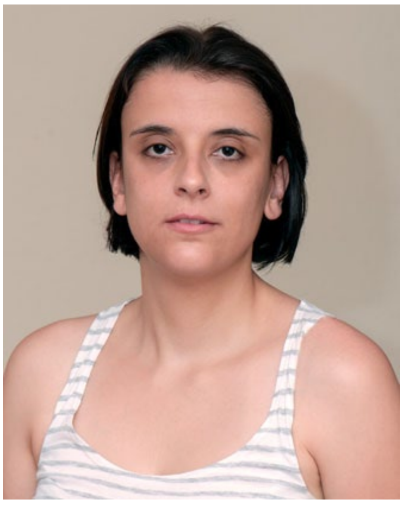

1. Introduction

Metal oxides encompass a very large family of solids reported in structural databases. This extreme versatility in compositions and structures yields a wide range of properties. These properties are very often combined to stability under ambient atmosphere to set the foundations for an extended range of applications. While the family of bulk oxides is still expending, nanoscaling offers an additional dimension to tune or to discover properties.

The relevance of nanostructuration for oxides is demonstrated by many application fields pertaining to nanoparticles like e.g. nanomedicine,[1] catalysis,[2] energy conversion and storage.[3] It is also well exemplified by the field of oxide epitaxial thin films. Indeed, planar deposition techniques offer a mature and versatile toolbox to deposit various oxide films and assess the role of nanoscale dimensions on magnetotransport and magnetism.[4] It is also providing interesting models to study the mechanisms of catalytic and electrocatalytic[5–7] reactions over oxides, including the structural and chemical modifications occurring at the oxide surface during these reactions. Epitaxial thin film deposition can also be used to finely tune the structural features of the oxide film. For instance, the strain can be adjusted by lattice mismatch with the substrate and the nanoscale thickness as well as the interface can be used to stabilize compositions that are very difficult to isolate otherwise or even not reported at the bulk scale.[8–10]

Nano-objects as nanoparticles, nanowires and 2D materials offer other possibilities than epitaxial thin films: adjusting the dimensionality enables probing the effect of nanoscale sizes on properties such as surface plasmon resonance,[11] and developing free-standing nano-objects that can be suspended in liquids opens the way to processing by using the nano-objects as building blocks of larger structures.[12] Growth of epitaxial thin films of complex structures and compounds, like many multicationic oxides, is well controlled because the conditions of pressure, temperature and strain conditions enable the growth on well-chosen substrates that act as seeds, thus limiting the energy input required for the nucleation of the compounds, which is typically achieved for bulk oxides by solid-state reactions above 1000 °C. The synthesis of free-standing nano-objects of such compounds becomes a challenging task as we cannot benefit from the advantages of epitaxial substrates. This may be one of the reasons why the range of oxides reported as nano-objects is very limited compared to the wide compositional and structural range of bulk oxides. Especially, most works on nano-objects have focused on crystal structures achievable at low temperature, and/or on simple compositions, especially single cation oxides. The other oxides, which may be qualified as "complex" in terms of structure and/or composition, have mostly been left aside. As many bulk complex oxides or oxide thin films show unique magnetic, electronic or spin properties, it is of utmost fundamental, if not applied, interest to assess how these properties can be impacted by decreasing dimensionality in nano-objects.

Achieving the synthesis of nano-objects of oxides that have been only reported in the bulk state or as thin films calls for the use of advanced synthesis methods that can yield free-standing nano-objects. Last years have seen a tremendous boost in this effort. Techniques that could have been considered as traditional, such as the sol-gel process, aqueous precipitation and colloidal syntheses in organic solvents have been revisited to be applied to nanomaterials pertaining to the family of complex oxides, while new approaches, including high temperature inorganic solvents and dedicated solid-state reactions have been developed to reach new oxides at the nanoscale. In this chapter, we aim at providing an overview of such recent advances, with an emphasis on new or revisited synthesis approaches and on the link between the targeted compounds and the chosen synthesis conditions.

We use three large case studies: multicationic oxides, oxides of titanium and tungsten bearing uncommon metal oxidation state or crystal structure, and crystal structures that have been discovered only in nano-objects. By addressing these wide families of solids, we deal with specific synthetic questions: how to obtain controlled nano-objects with low cost and environmentally friendly aqueous media? What strategies, relying on crystal structure relationships, can we use to target solids bearing transition metal oxidation states poorly stable in aqueous or organic media? How to drive reaction pathways towards unexplored areas of composition and structure maps? We will mostly show that answers to these questions can be found by reinvestigating aqueous precipitation processes, colloidal chemistry in organic solvents, the coupling of the sol-gel process with high temperature treatments and hard templating, as well as the exploration of molten salts as high temperature liquid media. We will discuss the underlying mechanisms, that encompass dissolution-recrystallization but also a range of reactions within nano-objects, including topotactic transformations by cation exchange, exfoliation, and reduction.

2. Multicationic oxides

2.1 Layered oxide-based materials

Two-dimensional oxides have attracted considerable attention in the last years owing to the properties derived from their layered structures. The capacity to store and/or to exchange species in the interlayer space, as well as the high accessibility to the catalytic active centers, make them interesting in energy storage and catalytic applications.[13,14] We choose herein two illustrative examples of layered oxides with simple composition: nickel and cobalt hydroxides. Solids derived from both elements are disclosed later with the aim of searching more advanced materials with multicationic compositions.

Layered nickelates show several structures that can be obtained as a function of the nickel oxidation state as well as of the synthesis conditions. α-$Ni(OH)_2$ is a kinetic reaction intermediate obtained by precipitating Ni^{2+} in basic aqueous solution, commonly NaOH or NH_3. This polymorph evolves to most stable β-$Ni(OH)_2$ by aging in aqueous media or heating in basic conditions.[15]

Both α-$Ni(OH)_2$ and β-$Ni(OH)_2$ are composed of $Ni(OH)_2$ layers. In α-$Ni(OH)_2$, water or intercalated ions are located between these layers while no space is available in β-$Ni(OH)_2$ for accommoding these species.[15] Doping the layers with other elements, such as trivalent aluminum, has increased the α–polymorph stability.[16] In this case, the positive charge introduced in the layers is compensated by the interlayer anions that remain strongly bonded. Likewise, the ability to intercalate cations in the interlayer space is of high interest for the electrochemical properties of α-$Ni(OH)_2$ as positive electrode in alkaline batteries[17] or electrocatalyst for the oxygen evolution reaction (OER).[18,19] Indeed, the substitution of nickel with small amounts of iron, incorporated on purpose or from an impurity in the electrolyte, produces one of the most active materials for the OER.[19,20] Additionally, ultrathin Ni(0)-embedded α-$Ni(OH)_2$ heterostructured nanosheets obtained by solvothermal synthesis have shown remarkable activity in hydrogen evolution reaction (HER) and OER electrocatalysis.[21] These performances have been shown to arise from the Ni(0)-Ni(II) active interface and the Ni(II) defects respectively, making Ni(0)/α-$Ni(OH)_2$ heterostructures highly interesting as durable and precious metal-free electrocatalysts for water splitting.[21]

Oxyhydroxides of Ni(III) can be obtained by precipitating a nickel(II) salt in basic and oxidizing conditions.[22] β-NiOOH and γ-NiOOH polymorphs are common positive electrodes of alkaline batteries through the redox couples β-NiOOH/β-$Ni(OH)_2$ and γ-NiOOH/γ-$Ni(OH)_2$, respectively**.**[23]

Inspired by methodologies of metal-organic frameworks (MOF) crystallization, a one-pot synthesis of single-layered metal-organic nanoribbons built from nickel-oxo octahedral clusters was accomplished.[24] For this purpose, alkyl benzene monocarboxylate was used instead of rigid arylic dicarboxylate linkers used for MOFs growth. The flexibility of the alkyl chain prevents conventional 3D growth, the monocarboxylate moieties acting as molecular spacers, pointing towards opposite directions. The inorganic clusters are bifunctionalized, which so that the four equatorial positions of the octahedral clusters can undergo condensation. This produces consecutive edge-sharing $NiO_4(OH)_2$ octahedra, forming inorganic chains which are separated by alkyl benzene monocarboxylate ligands at both sides of the inorganic nodes (**Figure 1a**). The inter-cluster separation can be controlled by modifying the length of the molecular spacer. Post-synthesis treatment in non-polar solvents allows the expansion of the ribbons, then the dispersion, and the exfoliation of the metal-organic 1D chains. These lamellar hybrid materials can be used to store and release in a controlled fashion non-polar active drugs such as semiochemicals (**Figure 1b**).

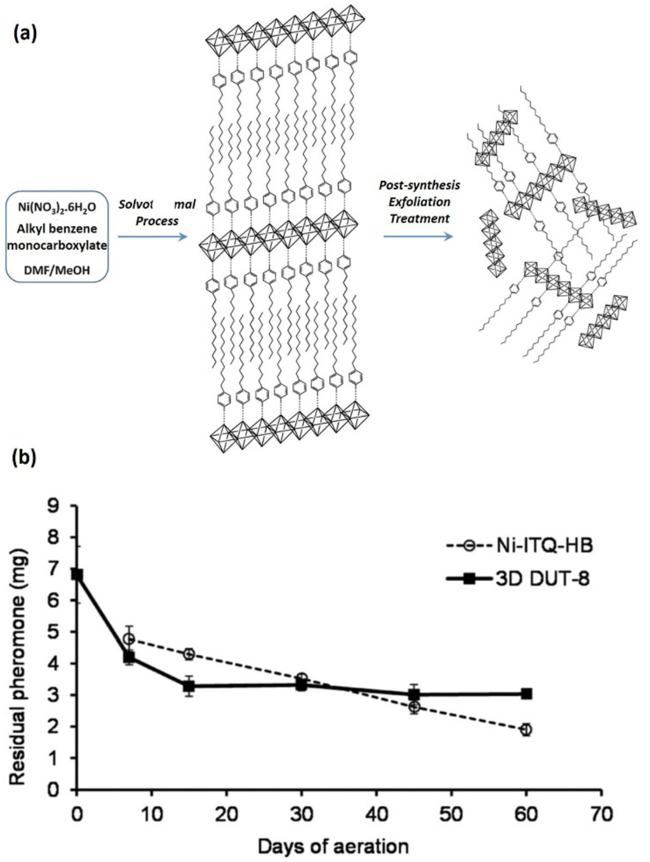

Figure 1. (a) Synthesis of layered NiO_6-based hybrid materials obtained after condensation and then after further exfoliation in apolar solvents and (b) Kinetics of the residual pheromone (3-(S)-methyl-6-(R,S)-isopropenyl-9-decenyl acetate) in the layered NiO_6-based hybrid material (Ni-ITQ.HB) and 3D DUT-8(Ni) MOF. Source: adapted from Moreno *et al.* [25] with permission of Wiley-VCH Verlag GmbH & Co. KGaA.

As for nickel, cobalt hydroxides exhibits two polymorphs: α-$Co(OH)_2$ and β-$Co(OH)_2$. Layered cobalt oxyhydroxides show significant deviations to stoichiometry that drive various behaviors. For instance, the spontaneous transformation of α-$Co(OH)_2$ to more stable β-$Co(OH)_2$ can be hindered by introducing exchangeable anions in the interlayer space that compensate the positive charge of the $Co(OH)_{2-x}$ layers.[26] Higher oxidation state phases related to α-$Co(OH)_2$ and β-$Co(OH)_2$ show also various conduction behaviors. Especially, β-CoOOH is insulating while γ-CoOOH is semi-metallic thanks to the presence of higher amounts of tetravalent cobalt that is concomitant to non-stoichiometry in the form of e.g. γ-H_xCoO_2.[27,28] The synthesis of cobalt oxyhydroxides is usually performed by treating cobalt (II) hydroxides under oxidizing conditions, indeed β-$Co(OH)_2$ and α-$Co(OH)_2$ evolve through topochemical transformations to β-CoOOH[29,30] and γ-CoOOH[28], respectively. The transformation of β-$Co(OH)_2$ to γ-CoOOH does not occur, unlike in the nickel hydroxides to oxyhydroxides transformations, probably because of the difference in iono-covalence of the M-O bond.[28]

Mixed nickel-cobalt oxyhydroxides have been synthesized with interesting capacities and electrocatalytic properties.[30–34] β-$Ni_{0.89}Co_{0.11}(OH)_2$ platelets of 20-30 nm diameter obtained by coprecipitation with ammonia show higher capacities compared to the cobalt-free materials as positive electrodes in Ni-based rechargeable batteries.[31]

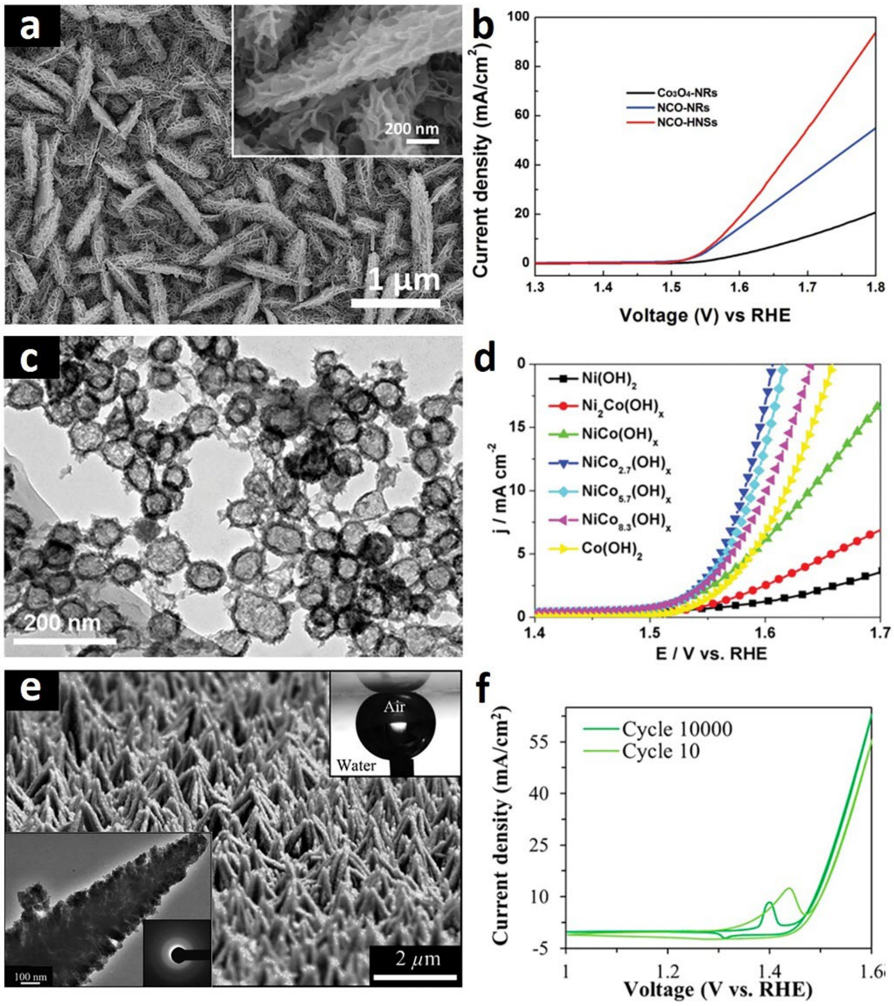

Figure 2. (a) FESEM image of Ni-Co oxide hierarchical nanosheets NCO-HNSs, (b) Linear sweep voltammetry cycles (LSVs) in OER conditions in basic media of NCO-HNSs, Co_3O_4 and Ni-Co oxide nanorods (Co_3O_4-NRs and NCO-NRs respectively), (c) TEM micrograph of amorphous Ni-Co hydroxide nanocages, (d) OER LSVs of amorphous Ni-Co hydroxide nanocages with several Ni:Co ratios, (e) SEM and TEM image of amorphous α-nickel-cobalt hydroxide nanodendrite forests. The inset shows the superaerophobic behavior of the material and (f) its corresponding cyclic voltammetry (CV) before (10 cycles) and after (1000 cycles) the accelerated stability test. Source: adapted from (a) Wang *et al.* [32], (b) Nai *et al.* [33] with permissions of Wiley-VCH Verlag GmbH & Co. KGaA and (c) Balram *et. al* [34] with permission of American Chemical Society, Copyright 2017.

Hierarchically structured mixed nickel-cobalt hydroxides have shown better performances than their non-structured counterparts in OER. Ni-Co (Co/Ni ratio 1/1) layered double hydroxides hierarchically composed by primary (smaller) and secondary (bigger) nanosheets (**Figure 2a**) obtained hydrothermally by urea hydrolysis, evolves to Ni-Co spinel through topotactic transformation by calcination. This Ni-Co oxide hierarchical nanosheets (NCO-HNSs) promotes more efficiently the OER in basic media compared to Co_3O_4 and Ni-Co oxide nanorods (Co_3O_4-NRs and NCO-NRs respectively) (**Figure 2b**). This activity enhancement arises by the synergy between the large surface area provided by the 3D hierarchical structure and the promotion of the formation of nickel oxyhydroxide on the surface that acts as OER electrocatalytic active species.[32]. Amorphous Ni-Co hydroxide nanocages with tunable composition (**Figure 2c**), synthesized using Cu_2O as template, also combine the high accessibility of the reagent with catalyst stability under *operando* conditions in OER in basic conditions, providing highly active an stable electrocatalyst (**Figure 2d**).[33] O_2 bubbles formation on electrode surface during OER can hamper the electrolyte-catalyst contact, thus decreasing the catalytic activity. To overcome this limitation, electrodeposited “forests” of amorphous α-nickel-cobalt hydroxide nanodendrites (**Figure 2e**) have been developed to exhibit superhydrophilicity and ensure excellent contact between the electrode material and the electrolyte and then to provide the catalyst with high activity and durability in OER (**Figure 2f**).[34]

In the search for further tuning of electrocatalytic properties, widening of the composition range of Ni-Co mixed layered compounds has been searched for. Nano-objects are ideal platforms for such a study because they accommodate larger strains than bulk materials. Hence, they might enable spanning a wide substitution range in $Na_{0.6}CoO_2$-based Ni-Co mixed oxides. $Na_{0.6}Ni_{0.5}Co_{0.5}O_2$ nanoflakes of 2-10 nm basal face and 1.5-3 nm thickness have been obtained through topotactic transformation starting from β-CoOOH and exchanging H^+ by Na^+

under soft conditions at 120 ºC (**Figure 3a-b**). Decreasing the particle size to this level allows surpassing the Ni solubility level achieved in the bulk state (Ni:Co 0.1:0.9 ratio).[35,36] The large surface area and the ability to preserve cobalt in high oxidation state (Co^{3+}/Co^{4+}) makes these materials highly active and stable in in OER (**Figure 3c-d**).[37]

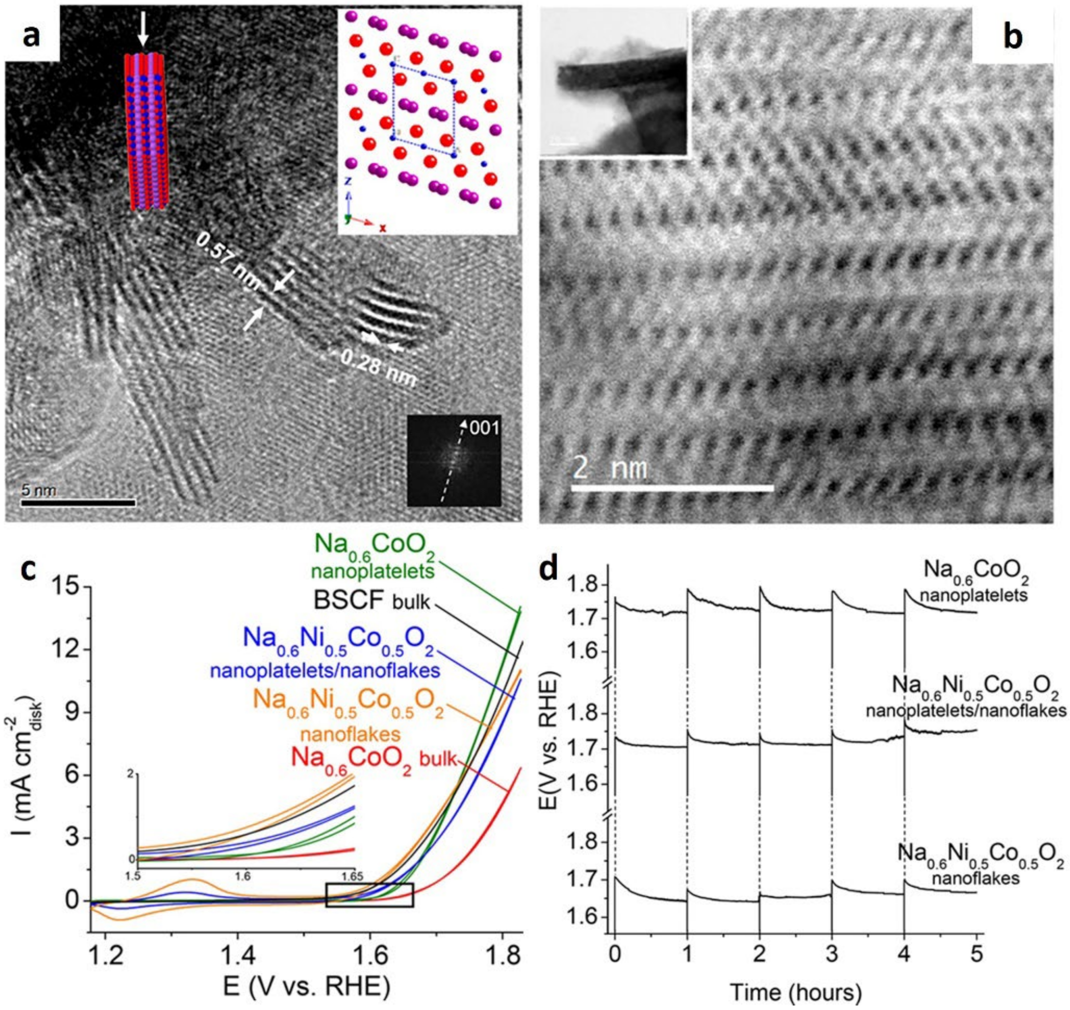

Figure 3. (a) HRTEM and (b) atomically resolved STEM images of $Na_{0.6}Ni_{0.3}Co_{0.7}O_2$, (c) CVs in OER conditions of sodium layered Ni-Co oxides with several compositions and morphologies, compared to reference bulk $Ba_{0.5}Sr_{0.5}Co_{0.8}Fe_{0.2}O_3$ (BSCF bluk) and (d) chronopotentiometry curves at current density 5 mA·cm^{-2}. Source: adapted from Azor *et al.* [37] with permissions of American Chemical Society, Copyright 2018.

Exfoliation of layered materials is also a good strategy for obtaining high-aspect-ratio nanosheets with high surface area, ideal for applications where the active surface plays a key role. A general strategy consists in a first proton exchange of the interlayer specie followed by amine intercalation. Successive intercalation of larger amines allows decreasing the interaction between layers and splitting them apart in colloidal suspensions. This approach has been successfully applied for lepidocrocite layered titanates,[38] protonated Ruddlesden-Popper phases,[39] layered manganates,[40] Aurivillius phase tantalates,[24] etc. Microwave heating fasten the exchange and intercalation steps[24] while selective centrifugation at different speeds allows the isolation of nanosheets with different levels of agglomeration.[41]

Layered $Mn_{1-x}Co_xO_2$ ($x = 0.2$-0.25) nanosheets have been synthesized following this exfoliation strategy.[42] $Na_{0.6}Mn_{1-x}Co_xO_2$ was acid-exchanged and then exfoliated with tetra-n-butylammonium cations yielding single-layer $Mn_{1-x}Co_xO_2$ nanosheets with 0.8 nm of thickness. Compared to other layered manganese and cobalt-based oxides obtained through bottom-up approaches, the material obtained by exfoliation shows larger lateral size and higher crystallinity, which is beneficial for electrochemical devices application. Indeed, these exfoliated nanosheets showed improved cycle performance compared to MnO_2 and higher capacitance than $Mn_{1-x}Ru_xO_2$ nanosheets in Li-ion batteries.

In this part, Ni and Co oxides have been discussed as illustrative examples of layered materials. Even showing simple composition, the corresponding hydroxides shows rich variety of structures obtained through control of the basic and oxidation-reduction synthesis conditions. Also, the versatility of organic moieties, such as monocarboxylates, allows the production of single-layered metal organic nickel oxide nanoribbons. Good control over morphology of the mixed Ni-Co hydroxides has been accomplished in aqueous synthesis conditions, with great implications in electrocatalytic applications. Finally, the more challenging synthesis of layered materials with complex compositions is illustrated with materials obtained through soft cation exchange or chemical exfoliation. The synthesis of these materials at the nanoscale enlarges the chemical composition in a range not achievable in the bulk state.

2.2 Oxidation states stables in organic media: the case of perovskites

$BaTiO_3$ is one of the most important perovskites because of its piezoelectric, ferroelectric and dielectric properties, which yield important applications in electro-ceramics and materials for optics.[43,44] The synthesis of $BaTiO_3$ by liquid-phase methods has allowed producing small and discrete nano-objects with different ferroelectric and dielectric properties compared to the bulk state, which depends on the crystal size.[44]

The first range of methods is aqueous-phase syntheses. Especially hydrothermal synthesis of $BaTiO_3$ is well known and the reaction mechanisms and kinetics have been deeply studied.[45–47] A barium precursor ($BaCl_2$ or $Ba(OH)_2$) and TiO_2 (usually amorphous or anatase polymorph) are mixed in a basic aqueous solution and heated under hydrothermal conditions, typically at 80-200 °C. Two synthesis pathways have been identified (**Figure 4**): *in situ* transformation and dissolution-reprecipitation. During *in situ* transformation, dissolved barium species react with suspended TiO_2 particles, forming a shell of $BaTiO_3$. Then Ba^{2+} diffuses through the particle until TiO_2 has completely reacted (**Figure 4a**). In the dissolution-reprecipitation pathway, $BaTiO_3$ crystallization goes through dissolution of TiO_2, formation of titanium and barium species that undergo condensation yielding homogeneous nucleation of the titanate or its heterogeneous nucleation at the surface of remaining TiO_2 (**Figure 4b**).[47]

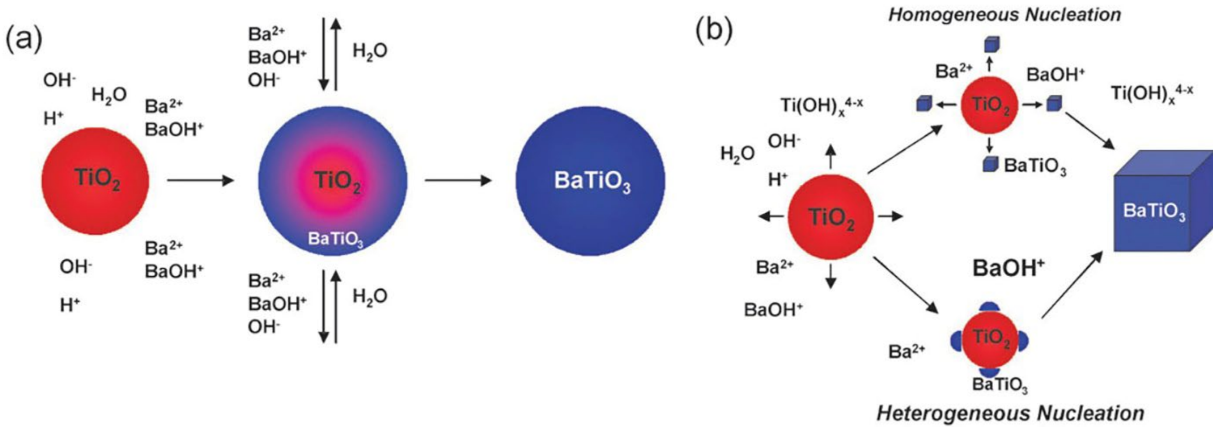

Figure 4. Hydrothermal crystallization mechanisms proposed for barium titanate: (a) *in situ* transformation and (b) dissolution-reprecipitation pathway where homogeneous nucleation occurs in the solution or heterogeneous nucleation occurs on TiO_2. Source: adapted from Modeshia *et al.* [45] with permissions of Royal Society of Chemistry.

The high versatility of hydrothermal synthesis allows the design of nanostructures with controlled morphology such as ultrathin nanowires [48] or nanotubes.[49] On one side, nanowires with high aspect ratio (more than 1300) and a diameter of less than 10 nm (**Figure 5a-d**) were synthesized using titanium alkoxide and barium hydroxide precursors dissolved in a basic aqueous-ethanol solution of polyethylene glycol and treated under hydrothermal conditions. The nanowires formation occurs through a combination of Ostwald ripening and cation exchange. Under solvothermal conditions, terbutyl titanate reacts with KOH producing $K_2Ti_8O_{17}$ intermediate. Then, potassium is exchanged by barium species in solution. On the other side, hydrothermal treatment of H_2TiO_3 exchanges H^+ with barium species in an aqueous-ethanol solution producing $BaTiO_3$ nanotubes.[49] Both materials show high microwave radiation absorption.[48,49]

The stability of Ba^{2+} and Ti^{4+} species allows the synthesis of $BaTiO_3$ in organic solvents, which provide access to a wide range of surface binding molecules – solvent or ligands – to control the particle size and shape. Organic solvents also enable the use of alternative soluble precursors compared to aqueous media, especially single source barium-titanium alkoxides.[50] 8 nm barium titanate nanoparticles with narrow size distribution could be readily obtained from such a single source precursor dissolved in diphenyl ether in the presence of oleic acid. The injection of hydrogen peroxide followed by heating at 100 ºC over 48 h was used to trigger the decomposition of the single source complex (**Figure 5e-f**). By increasing or decreasing the alkoxide/oleic acid ratio, the particle size could be tuned from 10 to 5 nm respectively.[50] Likewise, thermal decomposition of barium-titanium isopropoxide in heptadecane and in the presence of H_2O_2 yielded single crystalline barium titanate nanorods.[51] Solvothermal synthesis in a water-butanol mixture in basic conditions and in the presence of oleic acid also produced well faceted barium titanate cubes easily dispersable in nonpolar solvents.[52]

The high versatility of the benzyl alcohol solvent route was also instrumental in developing highly dispersible $BaTiO_3$ nanoparticles of 6 nm diameter (**Figure 5g-h**).[53,54] The synthesis mechanism involves Ti-O-Ti bridge formation *via* C-C coupling between isopropoxyl ligands and benzyl alcohol which produces 4-phenyl-2-butanol.[54] In such routes, benzyl alcohol plays the role of solvent, reagent and surface ligand (or precursor of surface ligand). Hence, the approach offers a very simple path by limiting the number of partners to introduce in the reaction medium.

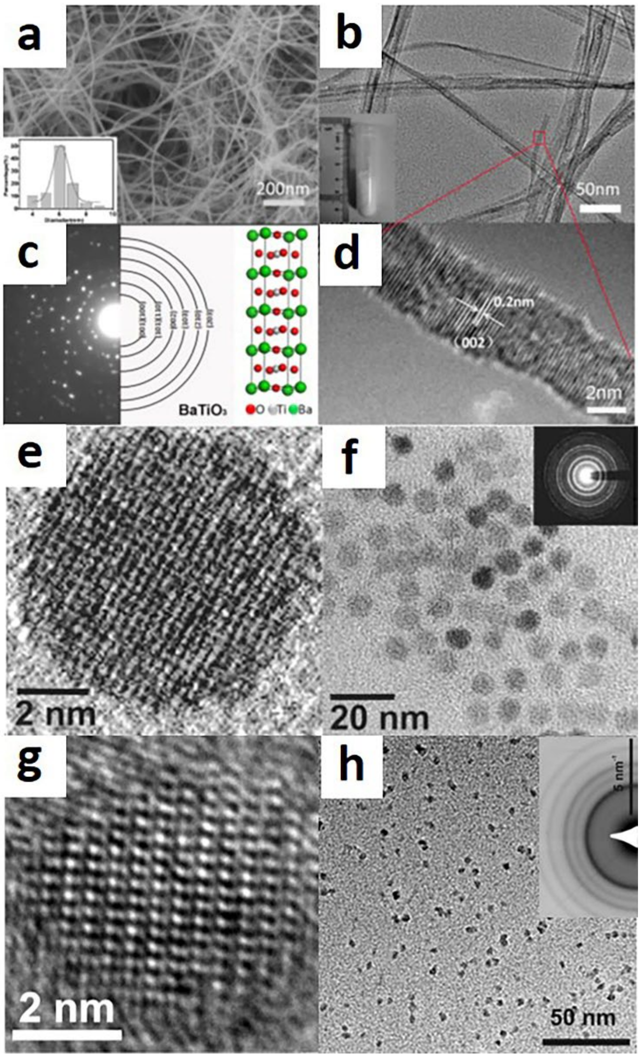

Figure 5. Electron microscopy images and selected area electron diffraction (SAED) of $BaTiO_3$ (a-d) ultrathin nanowires, nanoparticles obtained in (e-f) diphenylether and oleic acid and (g-h) benzyl alcohol synthesis. Source: adapted from (a-d) Yang *et al.* [48], Copyright 2013, (e-f) from O’Brien *et al.* [50], Copyright 2001 and (g-h) from Niederberger *et al.* [54], Copyright 2004, with permission of American Chemical Society.

Inorganic molten salts have also been employed to enable the production of well-crystallized barium titanate with several morphologies and controlled particle size. The synthesis of nanowires was first reported by using barium oxalate and anatase TiO_2 in molten NaCl with nonylphenyl ether additive as ligand. By treating this mixture at high temperature

(820 ºC), single-crystalline nanowires of ~50-80 nm diameter and 1.5-10 μm length were obtained.[55] One may however raise the question of the role of the organic ether molecule that is decomposed at the temperature of synthesis. The local temperature raise coming from ether combustion could favor the reaction. Hence, ligand-free synthesis of $BaTiO_3$ was performed in an equimolar NaCl:KCl mixture, again from barium oxalate and anatase. After treating the medium at 950 °C, $BaTiO_3$ nanostrips were obtained.[56] Barium titanate nanostructures with controlled morphology have been described by starting from TiO_2 with different nanoscale morphologies and by varying the nature of the Ba^{2+} precursor.[57] When spherical or rod-shaped TiO_2 reacted with $BaCO_3$ in NaCl:KCl eutectic mixture at 700 ºC, the morphology of the titanium precursor was preserved. On the other side when rod-shaped TiO_2 were reacted in the same conditions with BaO, cube-shaped $BaTiO_3$ particles were produced. The authors suggest that the difference in the morphology of the resulting powders arises from the difference in barium precursor solubility. $BaCO_3$ may be more soluble in the reaction media than TiO_2, thus directing the synthesis through *in situ* transformation that results in an isomorphic transformation of the particles, keeping the morphology of the less soluble component. On the other side the lower solubility of BaO, closer to TiO_2, gives the chance to break rod-shaped TiO_2 in several fragments before reaction with Ba^{2+} species, thus producing the particles with cubic morphology. Using the same synthesis protocol in the NaCl:KCl eutectic mixture from $BaCO_3$, $BaTiO_3$ particles with controllable size were obtained as a function of the thermal treatment (600-1000 ºC): the higher the temperature the larger is the particle size.[58] Well-faceted barium titanate nanocubes of 30-50 nm were obtained in softer conditions (200 ºC) by using more reactive solvent and barium precursors (NaOH and $BaCl_2$, respectively) and reacting them with TiO_2.[59]

This section has shown with the case study of $BaTiO_3$ that the synthesis protocols to reach nanostructures of multicationic oxides with common and stable metal oxidation states span a wide range of reaction media. The stability of the aforementioned cations enables the use of different reaction media for liquid-phase synthesis. If aqueous media rely on environmentally friendly protocols, organic solvents provide the ability to further tune nucleation and growth pathways, especially by enabling the use of a wide range of surface stabilizing species, solvent molecules or ligands. These species enable facile control of particle size and colloidal stability, and can drive growth of anisotropic shapes. If organic species cannot be used in high temperature inorganic molten salts, the latter however enable to a certain extent the control of particle faceting and shape, for instance by tuning the relative solubility of the reagents. Nonetheless, inorganic molten salts become an essential tool when one focuses on oxides bearing high oxidation state metal cations, which are not stable in organic media.

2.3 Oxidation states poorly stables in organic media: the case of perovskites

Organic solvents hold reductive properties that are not compatible with obtaining high oxidation state metal cations. This is especially the case of oxide perovskites bearing Bi^{3+} and Mn^{4+} cations: bismuth-based ferrates and manganates perovskites.

$BiFeO_3$ is an important multiferroic material, showing both ferroelectric and ferromagnetic properties at room temperature. These properties raise interest in memory devices, spintronics and sensors.[60–62] $BiFeO_3$ also exhibits interesting properties in photocatalysis. $BiFeO_3$ has been obtained through the Pechini process, by using tartaric acid as a complexing agent in an aqueous acid solution of bismuth (III) and iron (II) nitrates.[63] The resulting gel is then calcined under air. When citric acid is used instead of tartaric acid, $BiFeO_3$ is the minor phase accompanied by single cation iron and bismuth oxides as well as other bismuth ferrates. The authors suggest that the difference in phase selectivity arises from the ability of tartaric acid to form a heterometallic polynuclear polymeric network, which ensures a homogeneous mixture of the cations. Upon decomposition, this homogeneous gel yields the targeted phase. On the other side, citric acid forms dimeric bismuth complexes avoiding the formation of Bi-Fe heteronuclear complexes and thus yielding single-metal oxides. Similar approaches in the presence of ethylene glycol[61,62] produces $BiFeO_3$ nanoparticles because of the ability of ethylene glycol to crosslink the gel and to enhance the homogeneity of the cationic distribution. The particle size can be tuned with the calcination temperature.

Phase selectivity in the bismuth ferrate system has been accomplished under hydrothermal conditions. $Bi_{12}Fe_{0.63}O_{18.945}$, $Bi_2Fe_4O_9$ and $BiFeO_3$ micro and nanoparticles have been obtained with tunable morphology by adjusting the precursor ratio, the pH conditions or by adding H_2O_2.[64] Equimolar Bi^{3+}:Fe^{3+} starting solution in moderate basic (pH 8-12) media treated under hydrothermal conditions yields sillenite-type compound $Bi_{12}Fe_{0.63}O_{18.945}$ accompanied with $Fe(OH)_3$ that is easily removed by washing. Harsher conditions (pH 14, higher temperature (200 ºC) and H_2O_2 addition) equalize cation reactivity allowing the incorporation of both Bi^{3+} and Fe^{3+} in the same structure and yielding pure $BiFeO_3$. Similar results are obtained when starting with Bi^{3+}:Fe^{3+} 1:2 ratio in harsh conditions to produce pure $Bi_2Fe_4O_9$ without the need of adding H_2O_2.

Phase and size control have also been achieved by the addition of several mineralizers in the reaction media under hydrothermal basic conditions. Then, pure $BiFeO_3$, $Bi_2Fe_4O_9$ and $Bi_{12}(Bi_{0.5}Fe_{0.5})O_{19.5}$ can be isolated by adding K^+, Na^+ and Li^+, respectively.[65] Reactant solubility differences depending on the counter cation of the mineralizer could lead to differences in the dissolution-crystallization pathway, guiding the phase selectivity. On the other side, smaller particles are obtained when the mineralizer concentration is increased. Higher ionic strength may favor the nucleation at the expense of the particle growth.[65,66] Changing conventional heating by microwave-assisted heating yields well faceted $BiFeO_3$ cubes of 50-200 nm.[67] Sonochemical synthesis is also convenient for the selective synthesis of 25-30 nm $BiFeO_3$ cubes, allowing doping of the structure with other elements such as

Sc^{3+}.[60] Molten salts have also produced $BiFeO_3$ particles, but sizes could not be downscaled below the submicron scale.[68,69]

Besides bismuth, manganese also holds oxidation states not stable in organic media, especially Mn^{4+}. Mn^{4+} is often met in functional manganese oxide-based materials, so that its controlled incorporation in oxide nanostructures is of utmost important to control properties of catalysis,[70] electrocatalysis,[71,72] and magnetic properties.[73] Some attempts have been performed under solvothermal conditions, but they all required an additional calcination step at high temperature in order to crystallize Mn^{4+}-based compounds.[74,75]

In order to reach Mn^{4+}-based oxides through one-step liquid-phase synthesis, comproportionation of permanganate Mn(VII) and Mn(II) salts in water between room temperature and 250 °C has been proved as an efficient pathway.[76] This approach has been especially explored to synthesize rare-earth and alkali-earth manganite perovskites $Ln_{1-x}A_xMnO_{3-\delta}$ (Ln= lanthanide, A = alkali-earth metal cation and $\delta < 0.1$). The Mn(VII)/Mn(II) reagents ratio guides the final manganese oxidation state in the perovskite, and enables avoiding impurities.[45] Some studies suggest that the synthesis through aqueous-phase comproportionation at low temperature (< 300 ºC) with half-doped A site, is only thermodynamically possible with compositions corresponding to a Goldschmidt tolerance factor close to 1 and an A-site variance (cation disorder) closest to zero.[45,77] Other approaches able to work at high temperature for triggering perovskite crystallization, should overcome this limitation in the synthesis of perovskite at nanoscale.

The sol-gel process permits the synthesis of films,[78] ordered meso-/macro-structures,[79] and nanoparticles,[80–82] thus allowing the production of materials with relative high surface area and enhanced electrocatalytic activity, eg. in oxygen reduction reaction (ORR). Through a related approach, poly(methylmethacrylate) colloidal crystal templates have been used to produce three-dimensionally ordered macroporous $LaMnO_3$ with a surface area of ~20 m^2 g^{-1}. Good performances have been recorded in ORR electrocatalysis.[79]

Solid-state gelation has been developed recently to increase the surface area of $LaMnO_x$ aerogel up to 74 m^2 g^{-1}.[82] Preformed amorphous lanthanum oxide/Mn_3O_4 (core/shell) nanoparticles of 10 nm are deposited on carbon. Carbon acts as a continuous phase matrix promoting the gelation of the reaction medium. It is then removed upon further calcination, thus yielding a perovskite-aerogel formation. The resulting material shows high mass-normalized activity in ORR thanks to the high surface area achieved. This methodology has been extended to other perovskites compositions using various metal salts as precursors. Hence, $LaFeO_3$, $LaNiO_3$, $LaCoO_3$, $La_{0.5}Sr_{0.5}CoO_3$, and $La_{0.5}Sr_{0.5}Co_{0.5}Fe_{0.5}O_3$ could be obtained as nanostructured materials.

Synthesis in molten salts is a very interesting synthesis strategy to combine the advantages of the two above-mentioned strategies: on-step synthesis and high surface area of the resulting materials. The approach has been used to produce single crystal nano-objects with high crystallinity, controlled morphology and particle size. 20 nm $La_{0.67}Sr_{0.33}MnO_3$ well-faceted nanocubes were obtained using nitrate precursors and KNO_3 as solvent (**Figure 6a-b**). This nanomaterial shows large magnetoresistance at low temperatures. This behavior has been shown to arise from a 0.8 nm thick surface layer where manganese is partially reduced to a mixed Mn^{2+}/Mn^{3+} perovskite layer due to oxygen vacancies, independently of the spin polarization of the ferromagnetic core with the right oxidation state (**Figure 6c-d**).[73] The high crystallinity mimicking epitaxial thin films, the surface free of any organic ligands that could hinder charge transfer, and the relatively large surface area (36 m^2 g^{-1}) provide $La_{0.67}Sr_{0.33}MnO_3$ nanocrystals with high electrocatalytic activity and remarkable stability in ORR (**Figure 7c**).[72]

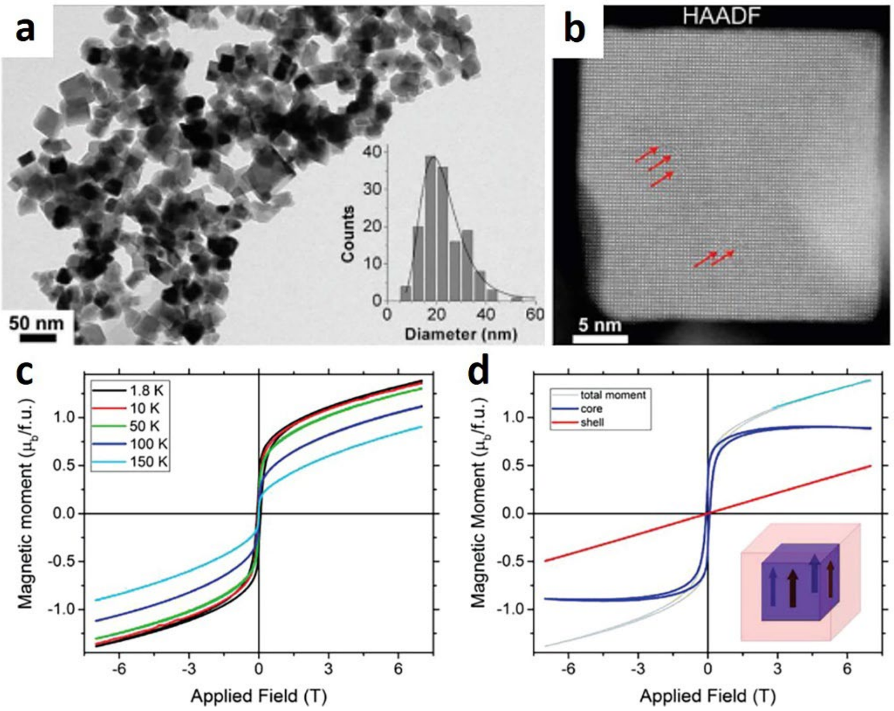

Figure 6. $La_{0.67}Sr_{0.33}MnO_3$ nanocubes obtained through the molten salts method (a) low magnification TEM and (b) STEM-HAADF images (c) magnetization curves at several temperatures and (d) decomposition of the magnetic signal. Inset: scheme of a core-shell nanocube, with well aligned core magnetic moments. Source: adapted from Thi N'Goc *et al.* [73] with permission of Wiley-VCH Verlag GmbH & Co. KGaA.

The high versatility of molten salts synthesis allows tuning the composition of well-faceted nanocubes, thus yielding not only $La_{0.67}Sr_{0.33}MnO_3$, but also $La_{0.67}Ca_{0.33}MnO_3$ or $La_{0.33}Pr_{0.33}Ca_{0.3}MnO_3$.[83] The phase selectivity could also be changed by adjusting the metal reagent ratio and by increasing the oxo-basicity of the molten salt used as solvent. Therefore, nanoparticles of the layered perovskite Ruddlesden-Popper phase $La_{0.5}Sr_{1.5}MnO_4$ could be synthesized in $NaNO_2$. The high oxo-basicity of $NaNO_2$ results in high amounts of O^{2-} released in the liquid medium, allowing the synthesis of the oxygen-rich $La_{0.5}Sr_{1.5}MnO_4$ phase at the nanoscale for the first time.[72] This strategy was also successfully applied to the synthesis of Sr-La-Ni perovskites. The high reactivity of nitrites compared to nitrates allows the synthesis of well faceted $LaNiO_3$ nanoparticles at lower temperature (200 ºC) as well as the synthesis of La_2NiO_4 and $LaSrNiO_4$ layered perovskite Ruddlesden-Popper nanoparticles.[84] The synthetic descriptors inferred in these works highlight the importance of the transition metal oxidation state, which governs the perovskite formation. The synthesis mechanism is directed by the reaction temperature: at low temperature topochemical transformation is preferred while at high temperature the energy input is high enough to promote a dissolution-reprecipitation pathway (**Figure 7 a-b**). This descriptor allows the design of nanoscaled perovskites with different activity and selectivity (number of electrons) in ORR (**Figure 7c**). [72,84]

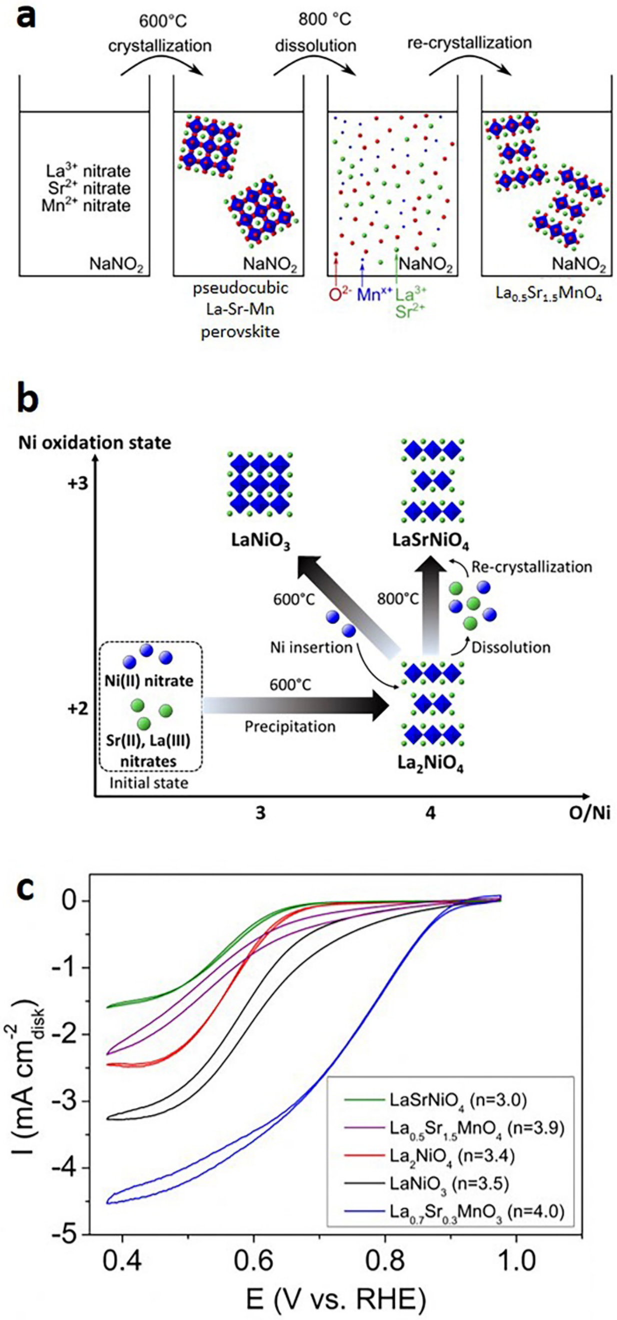

Figure 7. Proposed mechanisms involved in the synthesis of (a) layered $La_{0.5}Sr_{1.5}MnO_4$, (b) nickel-based perovskites in molten $NaNO_2$ and (c) CV in ORR conditions of the nanoscaled Ni and Mn-based perovskites obtained in molten salts (n= number of electrons involved in the ORR mechanism). Source: adapted from Gonell *et. al* (a) [72] and (b) [84], with permission of American Chemical Society, Copyright 2020. (c) Source: F. Gonell, from data in [72] and [84].

3. Oxides with uncommon metal oxidation states: the case of titanium (III) in oxides and extension to tungsten oxides

Titanium oxides have been paid attention due to their technological applications on a wide range of fields such as fuel cells, batteries, photovoltaics, photocatalysis and environmental remediation, among others.[85,86] The potential implementation of these oxides on different devices is due to their excellent chemical stability, corrosion and mechanical resistance, as well as their low cost, as titanium and oxygen are two of the most abundant elements on Earth.[87] The three main polymorphs of stoichiometric TiO_2 (anatase, rutile and brookite) are insulators with large electronic bangap (3.0-3.2 eV), limiting light absorption to the ultraviolet range of the solar spectrum. As a consequence, their potential applications in photocatalysis and photovoltaics are restricted. Nonetheless, partial titanium reduction, from Ti^{4+} to Ti^{3+}, gives rise to a modification of electronic, optical and charge transport properties related to crystal structure modifications. For photovoltaics, Ti^{4+} partial reduction is a promising approach for achieving narrower electronic band gap towards broader spectrum range absorption.[9,88] Likewise, similar positive effects, related with band gap decrease on TiO_2 polymorphs, have been observed in other properties such as photocatalytic water splitting.[87–90]

Traditionally, the most common approach for obtaining bulk reduced titanium oxides has been TiO_2 reduction at high temperature (≈1000 °C) by hydrogen or metallic titanium for a long period of time.[91,92] The properties and applications described above involve interactions between the material surface and other solution-phase or gas-phase species. As a consequence, developing synthetic approaches to decrease particle size is a suitable approach to probe the impact of the surface on the properties and possibly to enhance materials performances. A huge effort has been devoted to this trend by several groups during last years. With the aim of preventing the crystal growth, studies are focused on two kinds of approaches: encapsulating the precursors by templating to restrict particle growth, and exploring less energetically demanding processes by increasing the precursor reactivity, with the aim of decreasing the reaction temperature.

3.1. Crystal structures and requirements for the synthesis of oxides bearing titanium(III) species

To understand requirements in terms of synthesis conditions, it is instructive to scrutinize the crystal structures of oxides bearing titanium(III) species. Simple doping of Ti(IV) oxides is discarded from this discussion, as TiO_2 doped with Ti(III) as a consequence of oxygen vacancies or aliovalent cationic doping is poorly stable and readily undergoes re-oxidation to the stoichiometric compound. Likewise, related multianionic compounds, like barium titanium oxyhydride ($BaTiO_{2-x}H_x$)[93] have never been observed at the nanoscale to our knowledge and are not discussed in this chapter.

On the extreme range of oxygen stoichiometry with no Ti(III), TiO_2 exhibits several polymorphs. The Ti(III)-bearing compounds are all related to the rutile polymorph of TiO_2 (**Figure 8**). The rutile structure is built on TiO_6 octahedra sharing edges to form octahedral chains. These chains are linked together by sharing corners of their respective octahedra. Upon reduction of Ti(IV) by O^{2-} removal, one encounters Magneli phases of titanium with formula $Ti_{2n}O_{n-1}$. They were discovered in the 1950´s by A. Magnéli.[94] It is worth noticing that this kind of structure is not only established by titanium, but also by vanadium,[95] molybdenum[96] and tungsten,[97] although the two latter give rise to another general formula. For titanium and vanadium, the *n* value is usually accepted as an integer number between 3 and 10, however there are studies which suggest its maximum value could be higher.[98] The structure of Magneli phases $Ti_{2n}O_{n-1}$ can be understood by a thought experiment. Removal of O^{2-} from TiO_2 rutile would create unstable oxygen vacancies. To stabilize the structure and eliminate these oxygen vacancies, some TiO_6 octahedra would shift in order to share faces and form Ti_2O_9 octahedra dimers. This shift is accompanied by ordering of the dimers into shear planes and the formation of corundum structure blocks separating rutile domains (**Figure 8**).[86] Further reduction yields the corundum polymorph of Ti_2O_3, the most common polymorph that can be prepared in not highly demanding experimental conditions.[9]

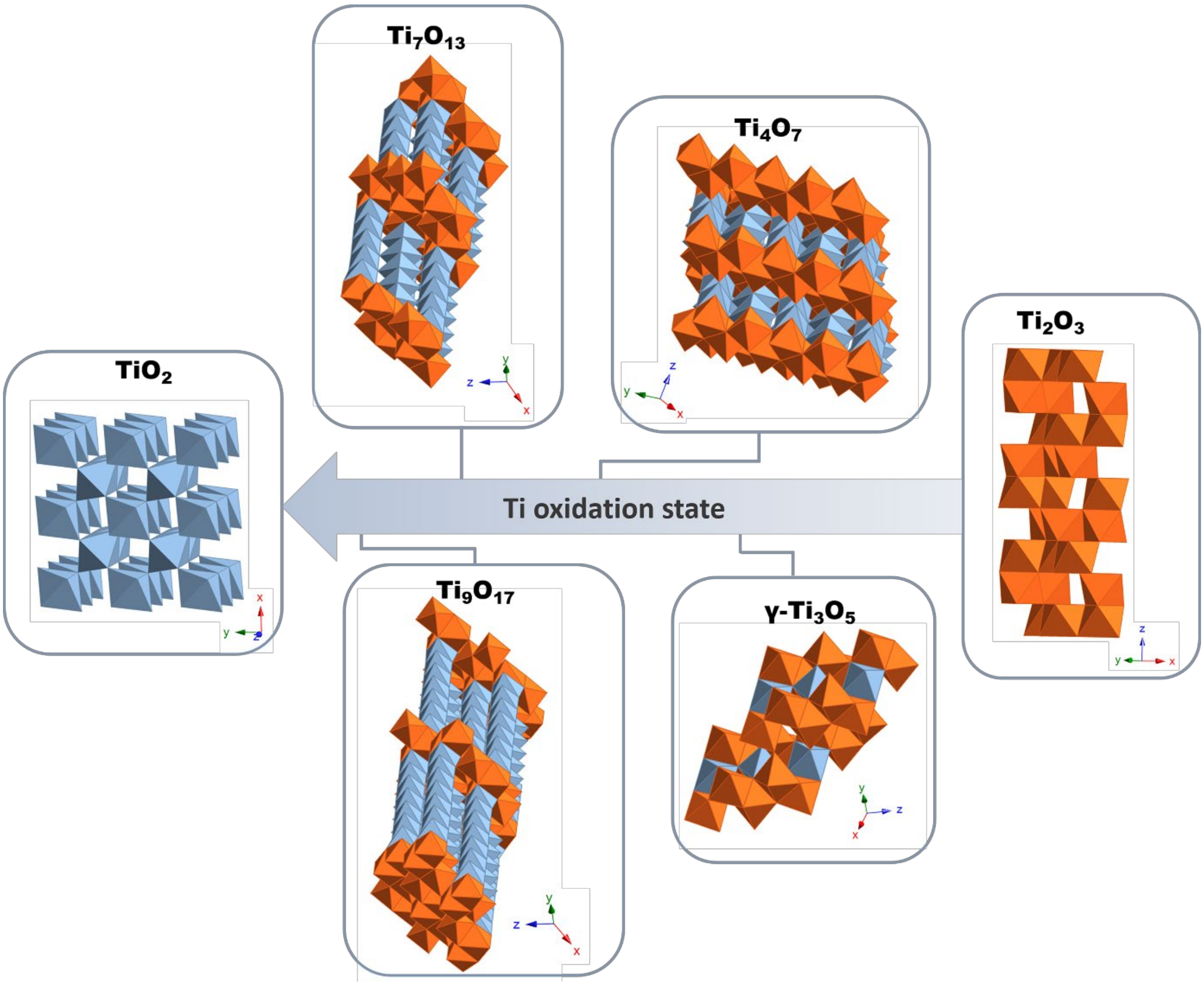

Figure 8. Schemes of the crystal structures of rutile TiO_2, corundum Ti_2O_3, and titanium Magneli phases. Face-sharing TiO_6 octahedra are plotted in orange. Source: Dr. Isabel Gómez-Recio.

Between Ti_4O_7 and Ti_2O_3, one encounters the few polymorphs of Ti_3O_5 (**Figures 8 and 9**)[99]. There are some ambiguities in the literature related with Ti_3O_5. Based on the general formula Ti_nO_{2n-1}, n=3, Ti_3O_5 could be included as the first member of Magneli phases. However considering the absence of crystallographic relationship involving the presence of shear planes, not all Ti_3O_5 polymorphs should be included in the family of Magneli phases.[99] The first studies of A. Magneli[100] described the two polymophs α and β (**Figure 9a**) with anasovite-type structures, related to each other by slight atomic displacements maintaining the symmetry and similar unit cell dimensions. The absence of crystallographic share planes on both polymorphs was interpreted as an anomaly among titanium Magneli phases, until γ-Ti_3O_5,[101,102] isostructural to V_3O_5, and δ-Ti_3O_5[103] were obtained, which are again related to each other by slight atomic displacements. γ-Ti_3O_5 (**Figure 8**) again shows face sharing octahedral related to shear planes and we then ascribe it to the family of Magneli phases. The last polymorph described, λ-Ti_3O_5 (**Figure 9b**)[104] shows a reversible photoinduced phase transition with β-Ti_3O_5. It should not be considered as a Magneli phase. As α-Ti_3O_5 and δ-Ti_3O_5 can be consider as β-Ti_3O_5 and γ-Ti_3O_5 distortions, respectively, their structures have not be included in **Figures 8** and **9**, for the sake of simplicity.

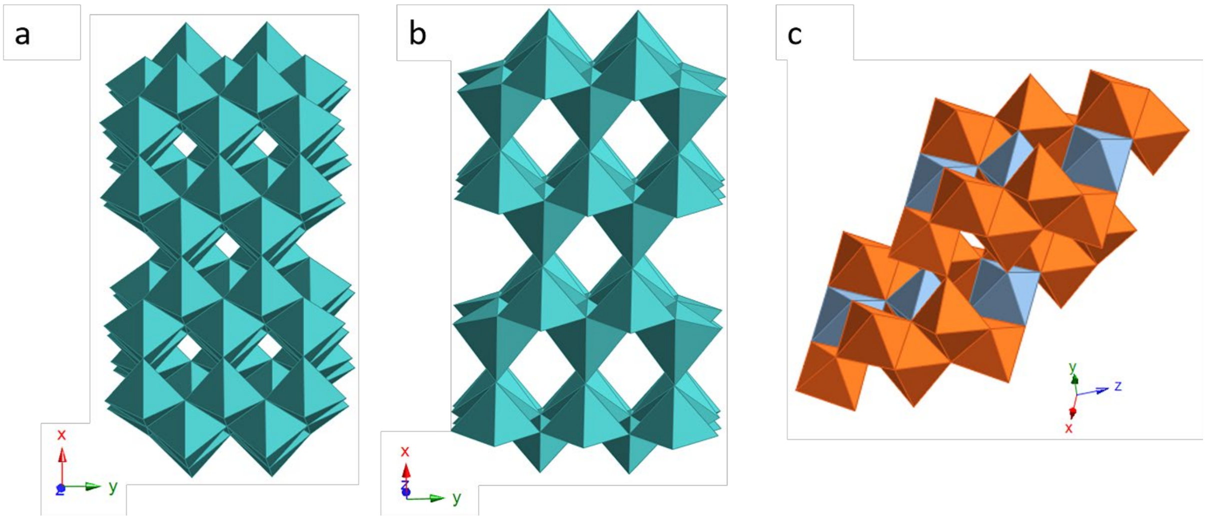

Figure 9. Schemes of the crystal structures of (a) β -Ti_3O_5, (b) λ -Ti_3O_5 and (c) γ-Ti_3O_5. Source: Dr. Isabel Gómez-Recio.

Overall, the structural relationship between some TiO_2 and Ti_2O_3 polymorphs and the Magneli phases highlights some guidelines for efficient syntheses of Ti_2O_3 and Ti_nO_{2n-1} ($n \geq 3$)

compounds, by considering most common TiO_2 as a starting material. First, the reduction of TiO_2 into Magneli phases and Ti_2O_3 can only proceed through the TiO_2 rutile polymorph, whether it is prepared on purpose or it is formed *in situ* during the reaction. In other words, the topotactic transformation of TiO_2 rutile is the only relevant reduction pathway towards Ti_2O_3 corundum or Magneli phases. This statement is supported by the outcome of reduction processes from the TiO_2 anatase polymorph. Indeed, the reduction of anatase does not yield the above mentioned rutile-related phases, but other materials, especially the so-called "black anatase".[105] Second, and as pointed out by Tominaka, Cheetham et al.,[106] the topotactic transformation from one phase to another involves collective atom displacements that are easier to trigger into nanomaterials than into bulk materials. Hence, nanomaterials are especially suited to explore such phase transformations and how they can yield full structural transformations while maintaining the overall shape of the nano-objects in so-called isomorphic transformations. In the following parts, we explore the current reaction pathways to trigger such transformations.

3.2. Ti_2O_3 nanostructures

The small bad gap (≈0.1 eV) of Ti_2O_3 corundum enables solar light absorption in the full visible range, which is improved in nanosized particles in comparison with bulk counterparts, as light scattering is enhanced with nanoparticles.[90] This characteristic accompanied by efficient solar-thermal conversion suggests that Ti_2O_3 can be used as photothermal material. Under light, the material could generate steam from water, as a first step in desalination or water purification, using sunlight as power source. As a proof of concept, Wang *et al.*[90] performed an experiment where Ti_2O_3 nanoparticles were deposited on a cellulose membrane at the surface of water (**Figure 10a**). After 15 minutes under light illumination, the temperature difference between the top and bottom part was 23 °C and water evaporation was observed (**Figure 10b,c**). In a reference experiment without nanoparticles, water was only heated by 0.5 °C, giving rise water evaporation rates between 2.65 and 4.18 times higher than pure water evaporation (Figure 10d,e)

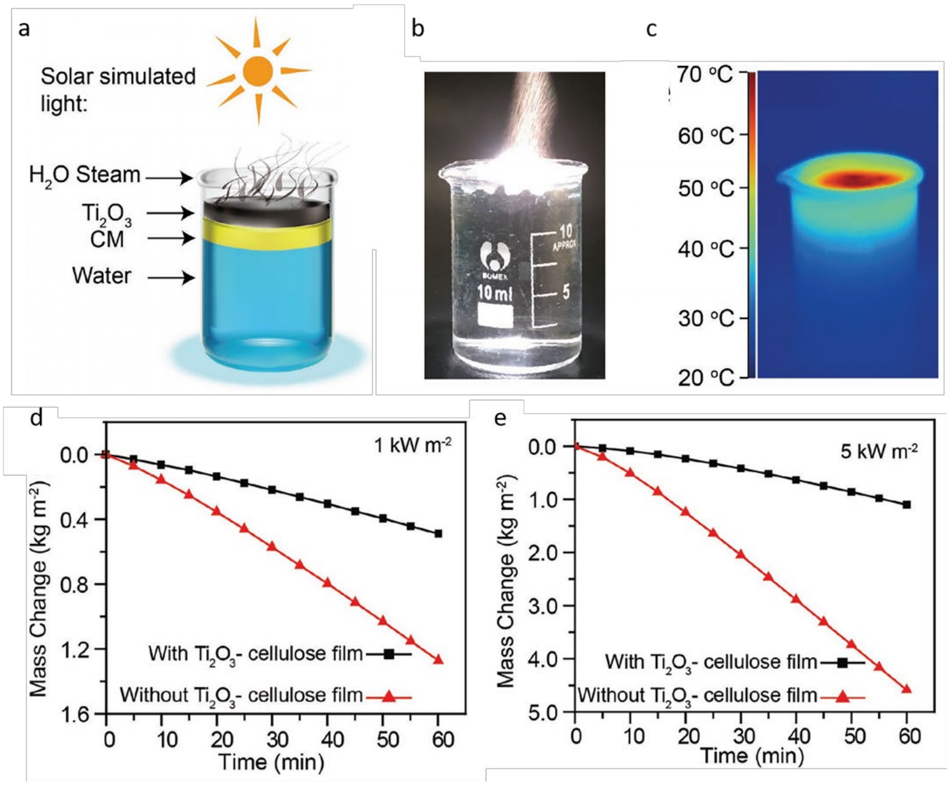

Figure 10. (a) Schematic set-up for proof-of-concept solar water steam production, (b) photograph of the water steam generation and (c) IR imaging of (b). Evaporation water weights against time with and without Ti_2O_3 thin-film device under the solar illumination, under 1 kW m−2 (d) and 5 kW m−2 (e). Source: adapted from Wang *et al.*[90] with permission of Wiley-VCH Verlag GmbH & Co. KGaA.

P. Zeng *et al.*[107] have coupled the sol-gel process with high temperature reduction to synthesize Ti_2O_3 nano- and micro-structures as cathode materials for lithium-sulfur batteries. Titanium glycolate microspheres (**Figure 11a,b**) were thermally decomposed into 1.5 µm rutile microspheres (**Figure 11c,d**) at 800 °C. Then, the TiO_2 microspheres were reduced into Ti_2O_3

microspheres (**Figure 11e,f**) by magnesium at 1000 °C. Upon reduction, the surface of the microspheres became faceted, showing clear crystal growth and microparticles as aggregates of nanoscale particles.

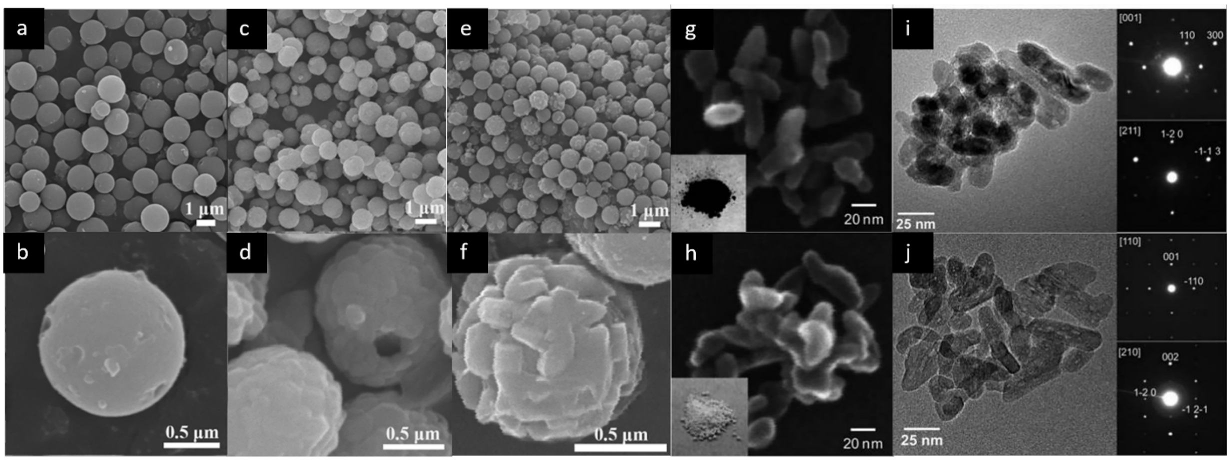

Figure 11. SEM images of (a,b) titanium glycolate, (c,d) rutile and (d,e) Ti_2O_3 microspheres. (g,h) SEM and (i,j) TEM images of (g,i) reduced TiO_2 nanoparticles and (h,j) corresponding TiO_2 nanoparticle precursors. The insets in are (g,h) photographs of the powders and (i,j) selected area electron diffraction patterns. Source: adapted from (a-f) P. Zeng *et al.*[107] and (g-j) S. Tominaka *et al.*[86] with permission of American Chemical Society, Copyright 2019, and Wiley-VCH Verlag GmbH & Co. KGaA, respectively.

Although solid-state synthesis usually yields bulk phases, S. Tominaka *et al.*[86,106,108] opened an elegant route for solid-state Ti_2O_3 nanoparticles synthesis. The authors were able to successfully reduce rutile TiO_2 nanoparticles into ca. 25 nm Ti_2O_3 nanoparticles (**Figure 11g-j**) by using different hydrides as low temperature reducing agents (350-420 ºC): CaH_2[86] and $NaBH_4$.[108] Shifting from calcium hydride to sodium borohydride enabled shortening the reaction time from 2 weeks to 24 h. Interestingly, it is possible to use such hydride-based reduction processes to trigger conformal transformations of TiO_2 nanostructures to Ti_2O_3 nanostructures, not only in nanoparticles,[86,106,108] but also in thin films and nanorods.[108]

Although extremely efficient in terms of morphology control, these hydride-mediated topochemical and isomorphic transformations do not enable a precise control of the composition, since an excess of hydride must always be used to ensure reduction of Ti(IV), thus yielding only the fully reduced Ti_2O_3.

3.3 Mixed valence Ti(III)/Ti(IV) oxides: Magnéli phases

In Magneli phases, the mixed valence Ti(III)/Ti(IV) ensures electronic conduction while corundum blocks scatter phonons, which decreases thermal conductivity without impacting strongly electrical conductivity **(Figure 12)**.[108] Ti_4O_7 (n=4) has a metallic behavior and is the most conductive phase of the Magneli titanium phase family (tabulated electronic conductive 10^3 S·cm^{-1}), comparable to graphite and metals.[109] When n increases, the proportion of Ti(III) decreases with $2Ti^{3+}$ for $(n-2)Ti^{4+}$ centers.

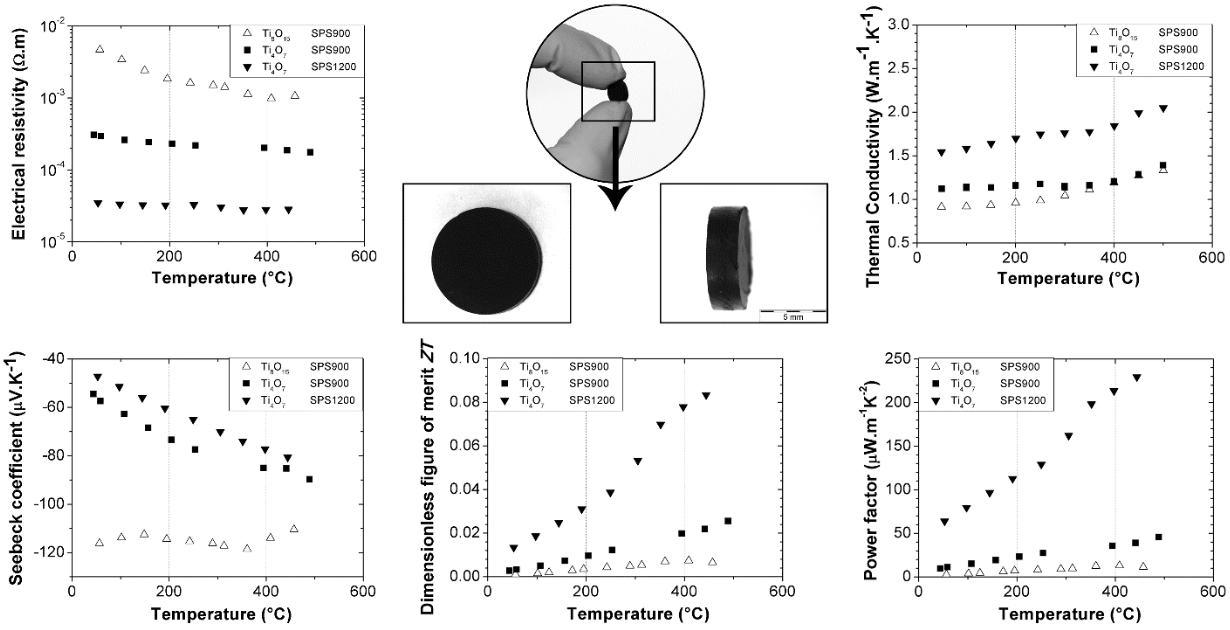

Figure 12. Picture of a Ti_4O_7 nanocomposite. Electrical resistivity, thermal conductivity, Seebeck coefficient, thermoelectric power factor and figure of merit for Ti_8O_{15} and Ti_4O_7 monoliths. Source: adapted from D. Portehault *et al.* [110] with permission of American Chemical Society, Copyright 2011.

Low thermal conductivity and large electrical conductivity are of interest for designing thermoelectric materials for power generation by recovering waste heat **(Figure 12**).[110–113] Magneli phases have also metal-semiconductor-insulator transitions, which can be controlled by external stimuli, as temperature, light and pressure.[87] Magneli phases of titanium are studied for electrochemical applications as fuel cells and batteries due to their mechanical and chemical resistance.[114,115] Due to their high electrical conductivity and chemical inertness, Magneli phases could indeed be alternative substrates to poorly stable carbon materials implemented in electrodes for Li-O_2 batteries.[114] Another field of interest arises from the expected affinity of sulfur for the Ti_4O_7 surface.[116–119] Ti_4O_7 nanostructured substrates have been designed, taking benefit from the strong adsorption of sulphur to enhance the stability of the sulphur electrode in Li-sulfur batteries.[116–119] Note however that these Ti_4O_7 materials showed surface contamination by carbon coming from the synthesis process (see *below*), which may have a big role in the adsorption of sulphur as well. Magneli phases are also studied in electrochemical wastewater treatment, as electrodes for the electrooxidation of pollutants such as dye methyl orange (**Figure 13**).[120,121] In all these prospective applications, increasing the surface-to-volume fraction ratio through nanostructuration is a viable approach to enhance performances.

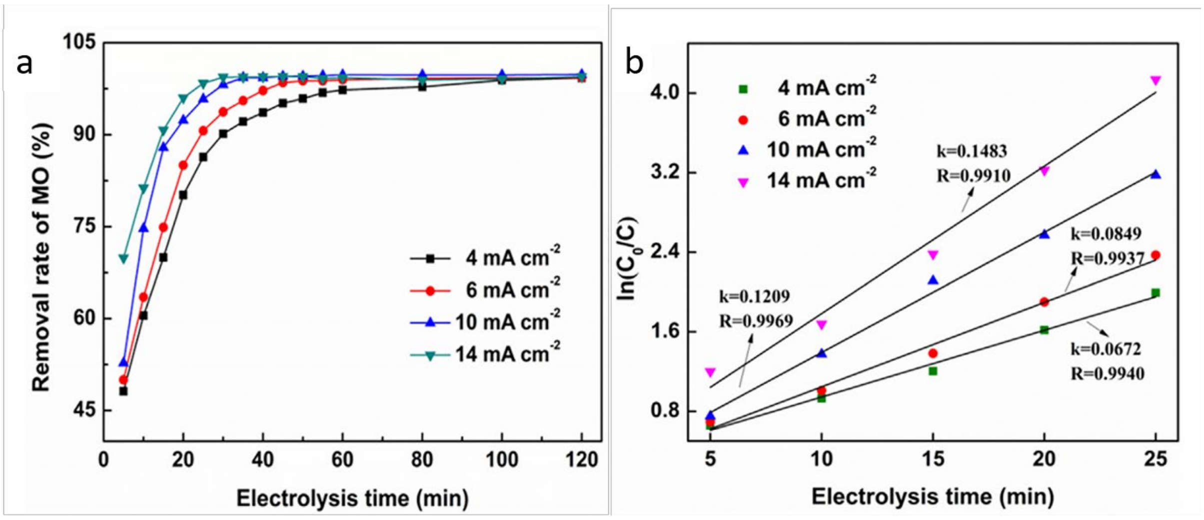

Figure 13. (a) Electrochemical oxidation of azo dye methyl orange by Ti_4O_7 at different current densities with (b) quasi-first-order kinetics fitting. Source: adapted from G. Wang et al. [120] with permission of Elsevier Ltd.

As discussed above, the most efficient way to envision the synthesis of nanostructured Magnéli titanium phases is to trigger topotactic reduction of TiO_2 rutile. Despite the observation by Tominaka *et al.*[86] of Ti_4O_7 as an intermediate phase during the solid-state reduction of nanoparticles of TiO_2 rutile into nanoparticles of Ti_2O_3 with CaH_2, which exemplifies the structural relationship described above in section 3.1, no report has shown yet the production of nanostructures of titanium Magnéli phases without using templating approaches. Indeed, the two strategies available to produce titanium Magnéli nanostructures rely on templating.

The first approach for the design of nanostructured Magneli phases is to simply consider the high temperature reduction of TiO_2 rutile by templating the TiO_2 nanostructure in order to limit grain growth and maintain nanoscale features. Y. Kuroda et *al.*[109] described a synthetic pathway for obtaining mesoporous Ti_6O_{11}. A colloidal crystal made of 50 nm silica nanoparticles was infiltrated by a solution of titanium precursor, followed by inorganic polymerization of this precursor to form a silica template-TiO_2 material. This material was reduced under H_2 at 800 °C to form the Magnéli phase Ti_6O_{11}, before dissolution of the silica template (**Figure 14a**). Although no structural characterization of the initial TiO_2 material is provided to assess the presence of the rutile polymorph, it is likely that it is present in the initial stage or formed upon heating during the reduction process. In a similar manner, X. Cao *et al.*[114] fabricated particles of Ti_4O_7 with average diameter of 300 nm, by H_2 reduction of TiO_2 nanoparticles coated by an ordered mesoporous SiO_2 shell. The mesoporous coating prevented Ti_4O_7 agglomeration and allowed diffusion of H_2 through the pores. Afterwards the SiO_2 shell was dissolved by an HF solution. This method was further refined by E. Baktash *et al.*[118] to be applied to 50 nm nanoparticles by combining silica templating with the use of anatase particles as diluting agent for limiting particle sintering. This method produces selectively Ti_4O_7 and Ti_6O_{11} nanoparticles of 50 nm by controlling the temperature of H_2 reduction, by taking advantage of the selectivity of topotactic reduction for the rutile phase, while the anatase component did not react with H_2. Finally silica and anatase could be selectively dissolved by HF (**Figure 14b**) to release 50 nm free-standing Magnéli nanoparticles.

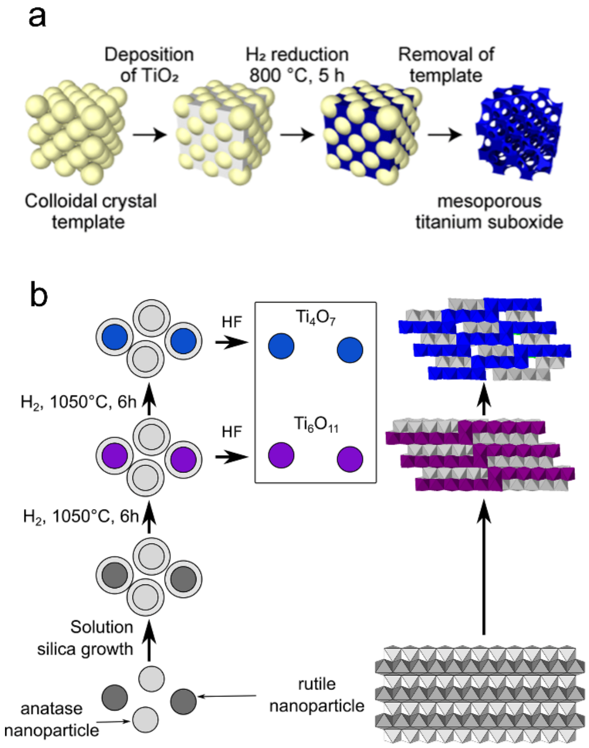

Figure 14. Schemes of silica templated syntheses of (a) mesoporous Ti_6O_{11} and (b) phases selective Ti_4O_7 and Ti_6O_{11} Magnéli phases. Source: adapted from (a) Y. Kuroda *et al.*[109] and

(b) E. Baktash et al.[118] with permission of Springer Science Business Media, LLC, part of Springer Nature and Wiley-VCH Verlag GmbH & Co. KGaA, respectively.

The second approach consists in using the template as a reducing agent. For this purpose, carbonaceous templates are used in order to trigger carbothermal reduction of TiO_2 rutile nanostructures. In these syntheses, the TiO_2 nanostructures and the template are produced concomitantly in a single step by using a sol-gel route (**Figure 15**). The initial reaction medium is a gel or a viscous solution made of a Ti(IV) alcoxide, a polymer and a volatile alcohol.[110] The condensation of Ti(IV) species is triggered by heating, yielding TiO_2 nanoparticles. Upon temperature increase under inert atmosphere, the polymer decomposes into a carbonaceous matrix embedding the particles. The matrix confines the particles and maintains their nanoscale size. In agreement with the topotatic transformation pathway, the rutile phase appears upon further heating after anatase formation in the early stages of TiO_2 crystallization. Ti_8O_{15} and then Ti_4O_7 crystallize after rutile formation, at 900 and 1000 °C, respectively. This approach enables implementing the various shaping methods applied with the sol-gel process.[12,122] This has been demonstrated by using electrospinning in order to produce nanostructured microfibers of different terms of Magneli phases (**Figure 15**).[123] These fibers show a specific internal structure, encompassing a carbon-free shell of large submicrometric particles and a core of nanoparticles still embedded into a carbon matrix. This observation highlights the need of the carbon template to limit particle growth and shows also a limit of this approach, since the reactivity of the template strongly depends on the gas flow near its surface, as the products of carbothermal reduction are gaseous CO and CO_2 species. The other limitation is the presence of carbon-byproducts at the surface of the Magnéli nanostructure, which can strongly modify the interaction of the material with the surrounding environment.[119,124]

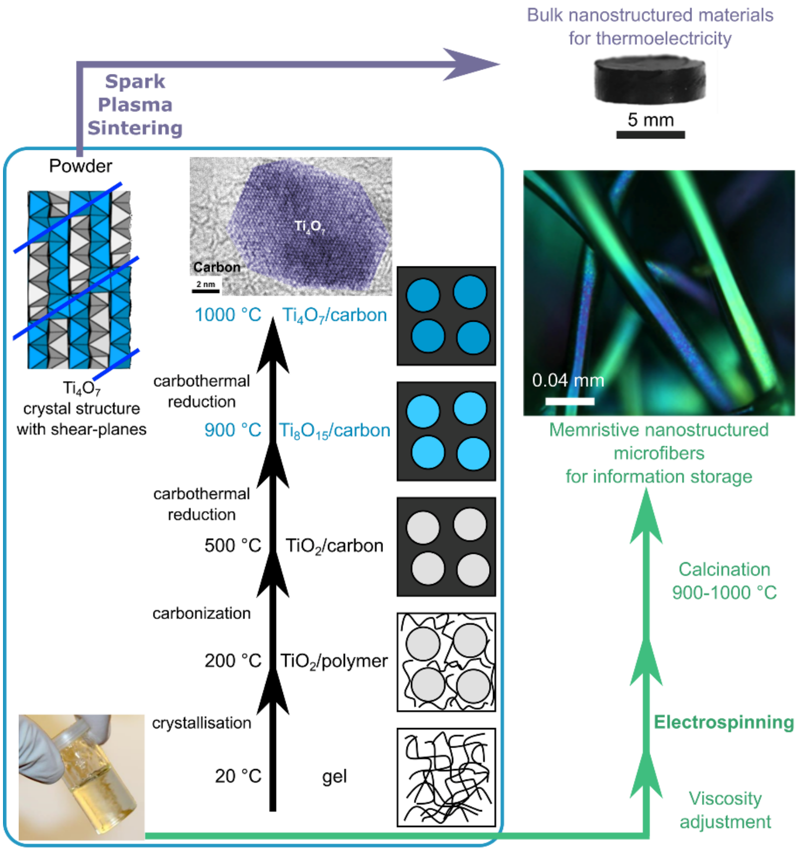

Figure 15. Synthesis and nanostructured processing of Magneli phases. Source: adapted from D. Portehault *et al.* [123] with permission of American Chemical Society, Copyright 2018.

3.4 Comparison to metal oxidation states stable in organic media: mixed W(V)/W(VI) oxides

Crystal structures based on shear planes are not only encountered in titanium oxides, but also with V(III)/V(IV), Mo(V)/Mo(VI), and W(V)/W(VI) oxides. The parent structure of molybdenum and tungsten Magnéli oxides is MO_3 (M = Mo, W) with the ReO_3 perovskite-related structure where the A site is empty and MO_6 octahedra are connected by corners.[125] Shearing leads to the formation of edge-sharing octahedra. Mo and W Magnéli oxides do not obey a general formula, although they can be described as M_nO_{3n-1}, M_nO_{3n-2}, M_nO_{3n-3}, M_nO_{3n-}

$_4$, M_nO_{3n-5}, etc. (**Figure 16**).[125] They are usually described as WO_x ($2.625 \leq x \leq 2.92$). For low reduction degree, ($x \geq 2.90$), shearing yields trimers of edge-sharing octahedra, while stronger reduction yields pentagonal columns of edge-sharing octahedra. Among W Magnéli oxides, only $W_{18}O_{49}$ has been isolated as a single phase. $W_{18}O_{49}$ nanostructures have also been extensively reported.[97,125]

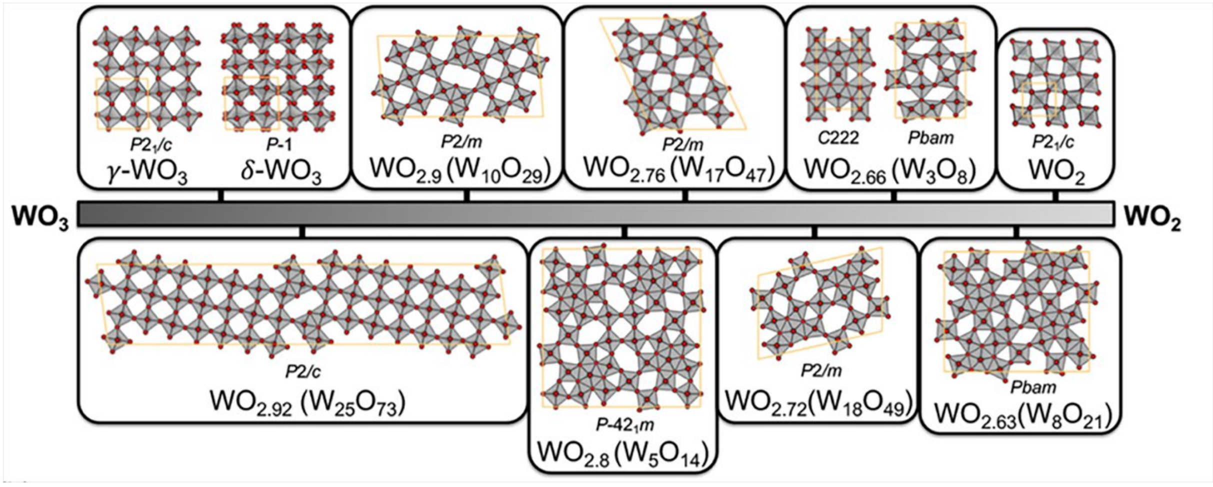

Figure 16. Stoichiometric and substoichiometric tungsten oxides. Source: adapted from Y. Lee et al. [125] with permission of American Chemical Society, Copyright 2019.

The gas sensing properties of $W_{18}O_{49}$ have been widely explored for the detection of reducing gases, as CH_4, NH_3, H_2 or H_2S, and of oxidizing gases, such as NOx or CO. The redox properties of the W(V)/W(VI) oxide are the key of the detection mechanism as redox reaction with the gas modifies reversibly the W(V)/W(VI) ratio and then the electrical conductivity of the material. This change of conductivity can be measured to enable quantitative evaluation of the analyzed gas (**Figure 17**).[126] The detection is enhanced by the high specific surface area of nanostructures, which drove efforts in their synthesis.

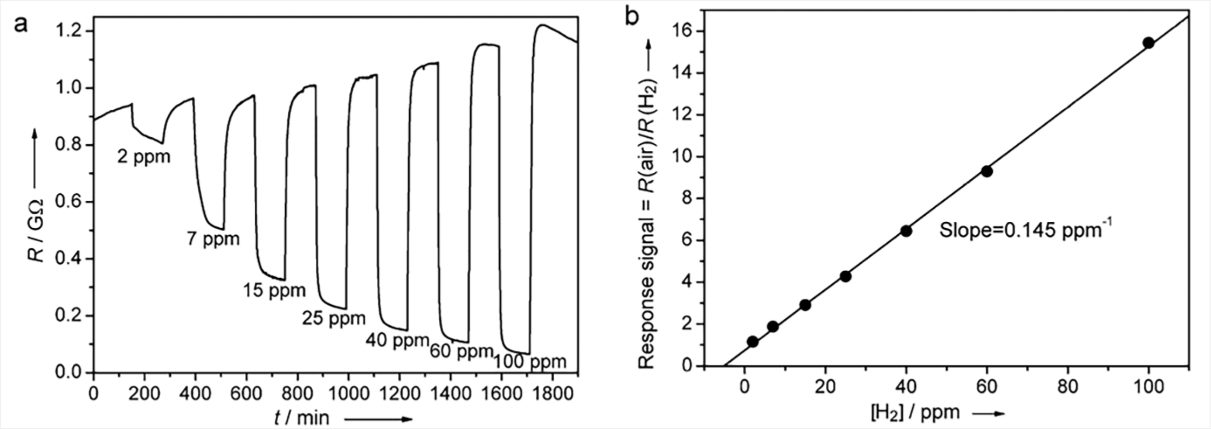

Figure 17. (a) Resistance change and (b) response signal of a $W_{18}O_{49}$ nanowire thin film with respect to various concentrations of H_2 at room temperature. Source: adapted from W. Cheng *et al.*[126] with permission of Wiley-VCH Verlag GmbH & Co. KGaA.

Owing to the strong oxidizing properties of W(VI), syntheses in organic solvents, often with reducing properties, usually do not result in stoichiometric WO_3, but in mixed W(V)/W(VI) phases, including $W_{18}O_{49}$. Solvothermal syntheses have been largely developed to reach nanostructures of this compound. One of the most efficient approaches is the synthesis in benzyl alcohol from WCl_6, that results in controlled growth of thin nanowires (**Figure 18**) with an optimized surface area to optimize the detection sensitivity.[126–129]

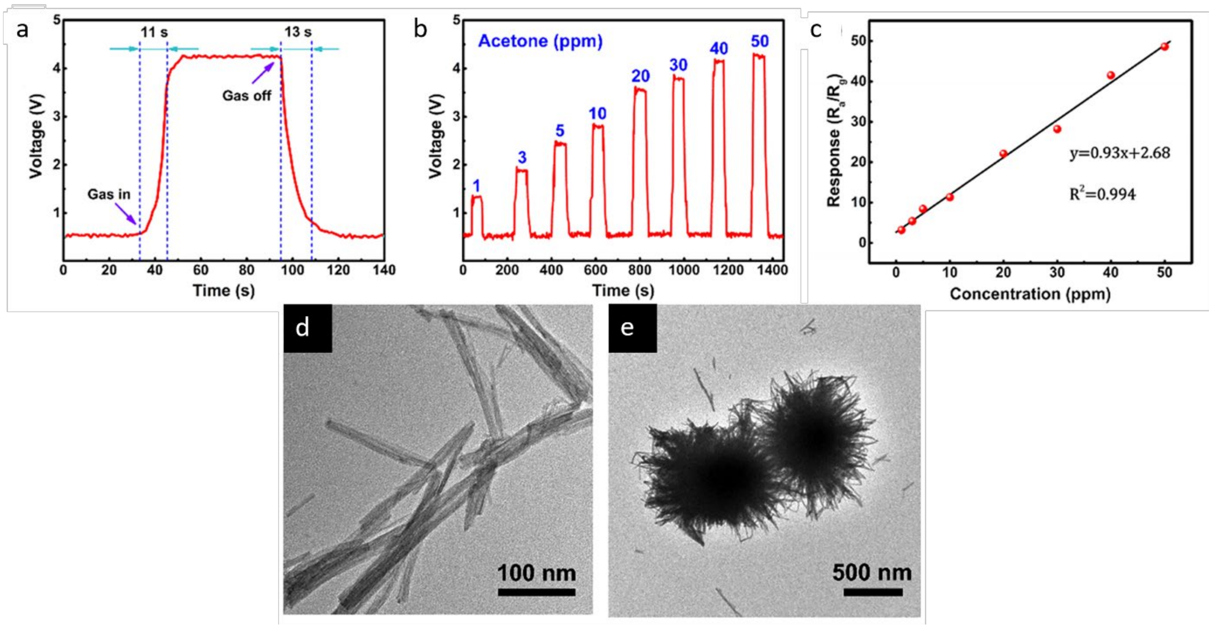

Figure 18. (a) Response and recovery curve of a $W_{18}O_{49}$-based sensor when exposed to acetone, (b) $W_{18}O_{49}$ detection response to different acetone concentration, (c) calibration of a $W_{18}O_{49}$-based resistive sensor of acetone, $W_{18}O_{49}$ (d) nanowire and (e) sea unchin-like nanoparticles. Source: adapted from W. Zhang et al.[129] with permission of American Chemical Society, Copyright 2020.

In the presence of alkali cations, the crystallization pathway proceeds differently, as alkali tungsten oxides spontaneously form. These so-called tungsten bronzes are formed by insertion of alkali cations into the host structure of WO_3. Hexagonal tungsten bronzes A_xWO_3 ($A = Na^+$, Cs^+, Rb^+ and NH_4^+ or even smaller hydrated cations as Li^+ and H^+) contain A^+ cations inserted in the hexagonal tunnels of the parent h-WO_3 phase (**Figure 19**),[130] delineated by 6 WO_6 octahedra sharing corners. Cation incorporation causes tungsten reduction, which is accompanied by color change from light yellow to deep blue,[131] as in Magnéli phases. This feature is largely exploited for the design of electrochromic devices, as smart windows or adjustable mirrors.[130,132,133]

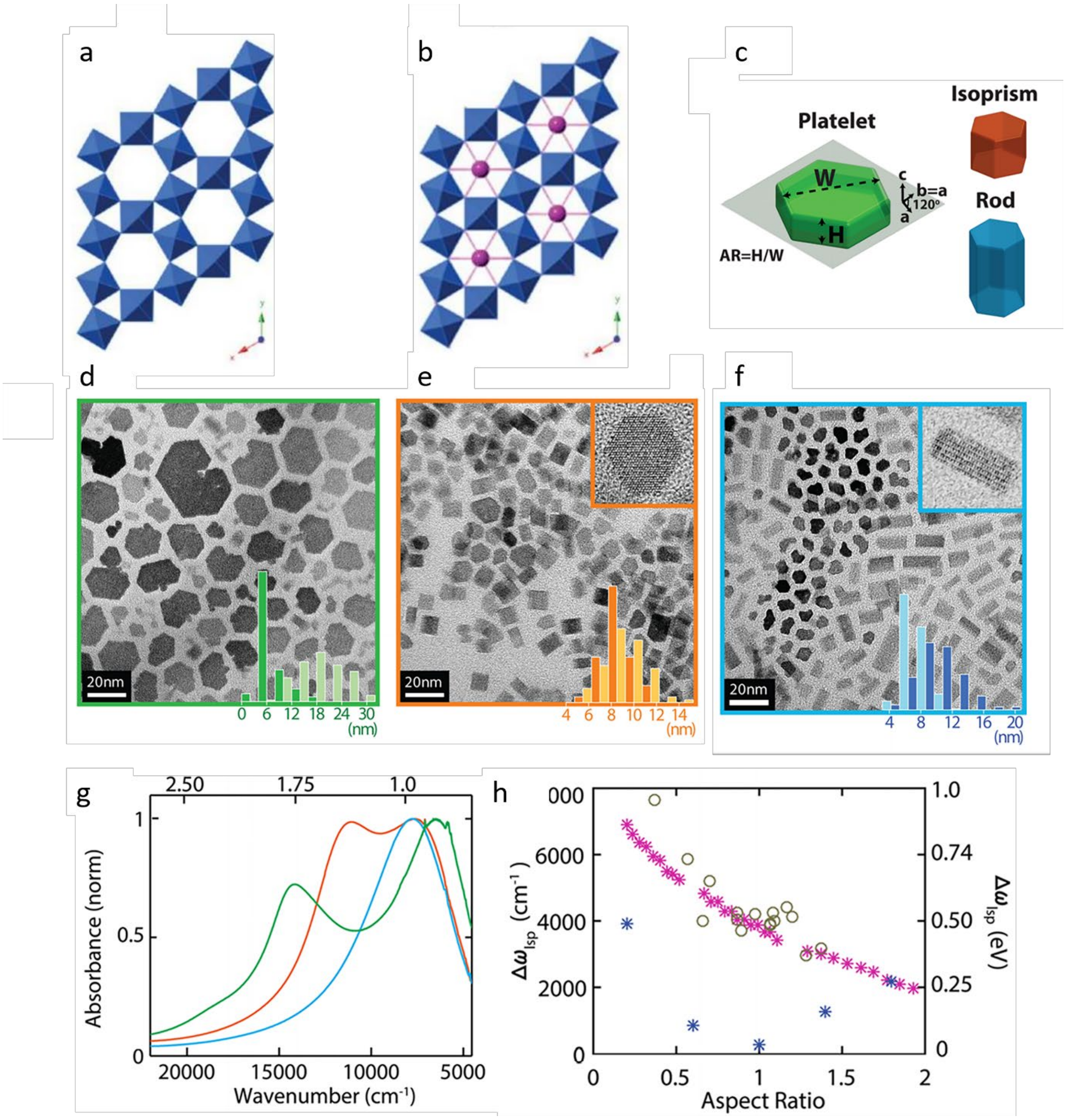

Figure 19. Crystal structure of (a) h-WO$_3$ and (b) M$_x$WO$_3$. Color code: W blue and M purple. (c) Schematic drawing of particle shapes corresponding to (d-f) TEM images. (g) Optical absorption spectra of h-CsWO$_3$ platelets (green), isoprisms (orange) and rods (blue) dispersed in tetrachloroethylene showing the aspect ratio dependence of LSPR. (h) LSPR peak splitting vs particle aspect ratio of nanocrystals (open circles) and by theoretical modelling assuming isotropic (blue stars) or anisotropic (pink stars) dielectric functions. Source: adapted from (a-b) T. Mattox et al.[130] and (c-h) J. Kim et al.[134] with permission of American Chemical Society, Copyright 2014 and 2016, respectively.

An interesting feature of nanoscaled tungsten bronzes is the emergence of surface localized plasmon resonance, a phenomenon related to collective oscillations produced by free or conductive electrons in large carrier density materials, in response to electromagnetic radiation which leads to a strong absorption in the near-IR or visible ranges, depending on the composition and morphology of the nano-objects.[11,135] On semiconductor materials, carrier density can be tuned by chemical doping, in such a way that the dopant type, concentration and distribution oin the crystal structure as well as particles morphology have an impact on the localized surface plasmon resonance (LSPR) response.[11] In this context, Manthiran *et al.*[136] described a plasmon shift and intensity decrease for $WO_{2.83}$ nanoparticles prepared by colloidal synthesis when they were treated thermally in an oxidizing environment, consistent with oxygen incorporation.

$WO_{3-\delta}$ has been mostly studied for its suitable energy band gap (2.6 eV) for interaction with visible light and for its stability in a wide range of conditions.[136] However while in bulk $WO_{3-\delta}$ color changes are related with oxygen deficiency and small cations intercalation, in nanoparticles the strong absorption in the near-IR (NIR) region is interpreted as a consequence of small polaron hopping and/or LSPR, as it has been reported for $WO_{2.72}$[137] and $WO_{2.83}$,[136] respectively. Polaron hopping is due to oxygen deficiencies that produces electrons trapped in 5d orbitals of tungsten atoms, followed by surrounding lattice polarization to generate polarons, which gives rise to polaron transitions between adjacent nonequivalent tungsten sites.[11,135]

To date, the studies about intense NIR absorption on $WO_{3-\delta}$ nanoparticles are still under discussion. As mentioned above, $WO_{2.72}$ color change has been interpreted as a result of polarons hopping process, nonetheless T. Masuda *et al.*[135] revealed an intense magneto-optical activity on $WO_{2.72}$ as consequence of circular modes of LSPR (magneto-plasmon). This magneto-optical behaviour is apparent from the differential absorption of left- and right-polarized light under a magnetic field. The magneto-optical activity of $WO_{2.72}$ nanoparticles exceeds the one of typical Ag nanospheres, which are among most promising candidates for plasmonic and magneto-plasmonic applications. Therefore, $WO_{3-\delta}$ will likely attract attention as low cost and high stability potential substitute to silver nanostructures.

Again, colloidal synthesis has proved highly efficient for the precise control of morphology and particle size for tungsten bronzes. Different nanoparticles of Cs-WO_3 have been obtained from solutions of WCl_4 and CsCl in mixtures of oleylamine and oleic acid heated at 300 °C.[130] By increasing the amount of oleic acid, more faceted particles were produced, in a manner that spheres, truncated cubes and hexagonal prisms were obtained.[130] Nanoplatelets with adjustable aspect ratio, as well as LSPR peak splitting (**Figure 19g,h**) could also be designed in a similar way by J. Kim *et al.*[134] by tuning reaction temperature, aging time and tungsten precursor degassing time (**Figure 19c-h**). Likewise, aqueous soft chemistry has allowed to stabilize thin nanoplatelets of a new $H_{0.07}WO_3$ hexagonal bronze structure (**Figure 20**), firstly reported by J. Besnardiere *et al.*[138] The optimal combination of nanoparticles morphology and framework preferential orientation give rise to promising electrochromic properties. Owing to structural tunnels perpendicular orientated versus the nanoplatelets basal plane, cation exchange properties are optimized in such nanostructures, enabling for instance reversible extraction of protons and fast electrochromic switching.

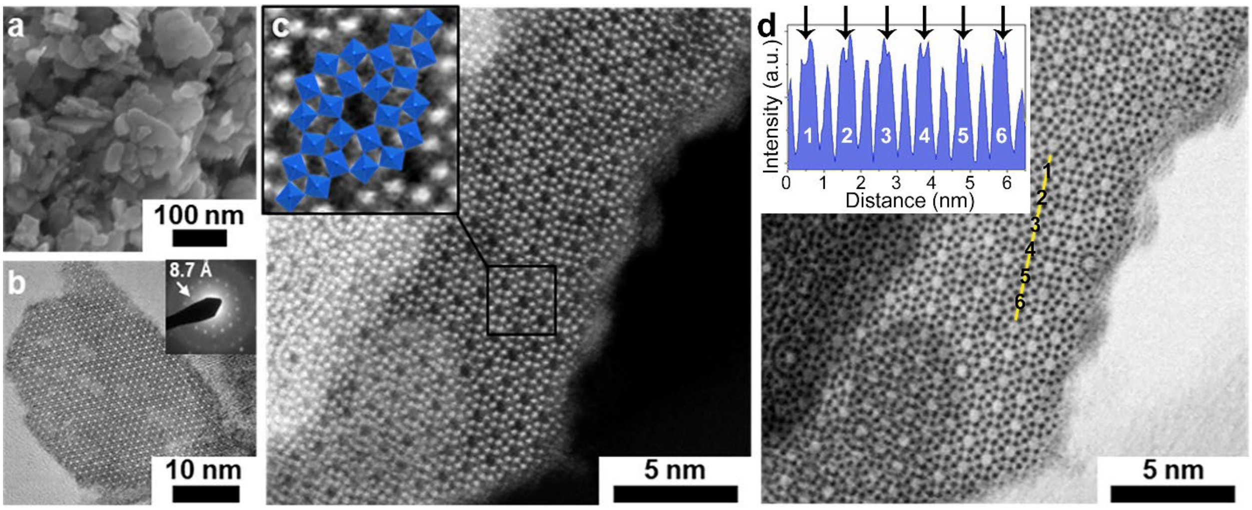

Figure 20. (a) SEM and (b) TEM images of $H_{0.07}WO_3$ hexagonal bronze nanoplatelets. inset in (b) shows a typical SAED pattern. (c) HAADF-STEM and (d) ABF-STEM micrographs showing the arrangement of tungsten octahedra (blue, inset of c). Source: adapted from J. Besnadiere *et al.*[138] with permission of Springer Nature.

A quick parallel between mixed valence titanium and tungsten oxides, especially Magnéli phases, shows that the crystallization of these structures is not occurring at the same temperature of synthesis. While tungsten Magnéli phases are readily obtained between 200 and 300 °C, to date no process has been suitable to reach titanium Magnéli phases below *ca.* 800 °C. The reason for this discrepancy has not been assessed to our knowledge, but one may attempt to provide several guidelines that could be useful for future investigation of these phases. A first obvious difference is the nature of the stoichiometric parent compounds. Rutile TiO_2 and ReO_3-type WO_3 show a different connectivity, as the latter is built only from corner-sharing octahedra while the former encompasses also edge-sharing octahedra. This difference is reflected in the relative stability of the compounds. This could explain why WO_3 is more prone to structural transformation than rutile TiO_2. Likewise, the shearing involved in the transformation of the parent phases into Magnéli phases implies the formation of edge-sharing octahedra for tungsten and of face-sharing octahedra for titanium. The latter may be related to larger activation energy, especially because it requires breaking some Ti-O bonds to enable shifting of Ti centers.

4. Stabilization of new crystal structures at the nanoscale

Upon decreasing of particle size, the surface-to-volume ratio increases, resulting in the exaltation of the contribution of the surface to the total enthalpy. Because creating a surface has an energetic cost, this surface contribution to the total free enthalpy is destabilizing. Nanostructures and nanoparticles are then intrinsically metastable. An important additional consequence of this surface effect is that at a given size, the extent of the destabilization depends on the nature of the facets exposed, but also on the crystal structure. Indeed, the surface enthalpy depends on the atomic arrangement of the surface, and then on the crystal structure as well. The result is that not all solids are destabilized by the same energy increase. Therefore, inversion of the relative stability order can take place. This effect is well known in the case of polymorphism, especially for TiO_2 where the bulk thermodynamic stable phase is rutile, while it becomes anatase below the crossover particle size, which is situated between 10 nm and several tenth or hundreds of nanometer.[139,140] Other examples of stability inversion at the nanoscale encompass the brookite polymorph of TiO_2, but also alumina and zirconia phases.[141] This trend is driven by the relatively general situation that (1) the difference in Gibbs free energy between polymorphs is of 1-10 $kJ\ mol^{-1}$, which is commensurate with the surface enthalpy when the particles are small enough ($\sim$1 $J\ m^{-2} \sim 8\ kJ\ mol^{-1}$ for TiO_2 of 100 $m^2\ g^{-1}$);[140,141] (2) the surface enthalpy decreases with increasing metastability, which often relates to decreasing density.[141] As a consequence, metastable phases in the bulk state may become the thermodynamic ones below a critical size. This explains not only why metastable solids are more easily accessible at the nanoscale, but also why exploring nanostructures with high surface area can give rise to the discovery of new structures. This field is described in the next paragraphs.

4.1.Hard templating to isolate bulk metastable oxides at high temperatures

Perhaps the earliest example of discovery of new compounds at the nanoscale is the case of ε-Fe_2O_3. It has been first reported in 1934,[142] then in the 1960s,[143,144] before being reinvestigated in the 1990s[145] when it became clear that an efficient pathway to this compound required templating into silica. 10 nm maghemite γ-Fe_2O_3 nanoparticles were embedded by a sol-gel-derived silica matrix. Upon heat treatment under air above 1400 °C, a structural transformation occurs in the nanoparticles that also slightly coalesce, yielding 30 nm ε-Fe_2O_3 nanoparticles (**Figure 21**). The material has been reinvestigated when its extremely high coercive magnetic field (2 T at room temperature) raised a large interest for data storage.[146,147] Few years later until very recently, other properties were identified for doped or undoped ε-Fe_2O_3, including efficient absorption of millimeter electromagnetic waves,[148] multiferroicity[149] and magneto-optical properties.[150] Further refinement of the encapsulating approach included the design of free-standing iron oxide-silica core-shell nanoparticles with 30 nm ε-Fe_2O_3 cores.[151] ε-Fe_2O_3 nanorods could also be designed.[146,152] Investigation of the energetic landscape highlighted that ε-Fe_2O_3 was an intermediate in the transformation from γ-Fe_2O_3 to α-Fe_2O_3 and was stabilized for particle sizes below ca. 30 nm, although the exact crossover size is still conversial.[152]

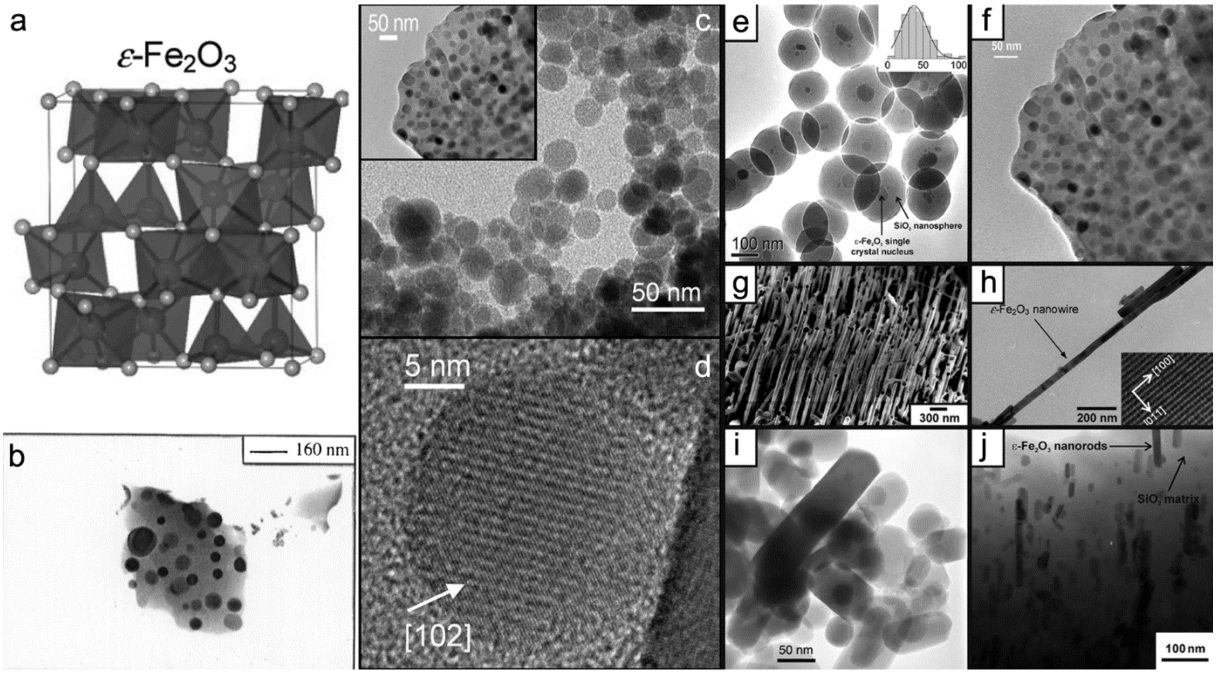

Figure 21. (a) Crystal structure of ε–Fe_2O_3, (b) and (c insert) TEM images of ε–Fe_2O_3 nanoparticles embedded in a silica matrix, (c) TEM and (d) HRTEM images of ε–Fe_2O_3 nanoparticles after removal of the silica template matrix (c insert). Spherical ε–Fe_2O_3 nanoparticles in silica (e) shells and (f) matrix. ε–Fe_2O_3 (g, h) nanowires and (i, j) nanorods. Source: adapted from (a) Sakurai *et al.* [153] with permission of American Chemical Society, Copyright 2009, (b) Tronc *et al.*, 145] with permission of Elsevier, Ltd., (c, d) Gich *et al.*[154] with permission from of IOP Publishing, Ltd, and (e-j) Tuček *et al.*[152] with permission of American Chemical Society, Copyright 2010, (e) Taboada *et al.* [151] with permission of American Chemical Society, Copyright 2009, (f) Popovici *et al.*[155] with permission of American Chemical Society, Copyright 2004, (g) Morber *et al.*[156] with permission of American Chemical Society, Copyright 2006, (h) Sakurai *et al.* [157] with permission with permission of American Chemical Society, Copyright 2008, (i) Kelm and Mader [158] with permission of Wiley-VCH Verlag GmbH & Co. KGaA, (j) Sakurai *et al.* [159] with permission of Elsevier, Ltd.

Another example of the templating strategy to isolate new oxide phase arising at the nanoscale is λ-Ti_3O_5.[104] Again, TiO_2 nanoparticles where produced while being encapsulated into a sol-gel derived silica matrix. Upon reduction by heating at 1200 °C under a dihydrogen atmosphere, λ-Ti_3O_5 was formed as 10 nm nanoparticles and added a term to the polymorphs of Ti_3O_5 (**Figures 8, 9** and **22**). The crystal structure of λ-Ti_3O_5 is maintained up to ~500 °C before it transforms into α-Ti_3O_5. λ-Ti_3O_5 also undergoes a reversible phase transformation to β-Ti_3O_5 triggered by high pressures or short light pulses.[104] Interestingly both polymorphs have very different colors, blue for λ and yellow for β. The authors took benefit of this property to design optical data storage devices.[104] Later, a carbothermal reduction pathway towards λ-Ti_3O_5 was also explored,[160] in a similar way as described above for Magnéli phases.

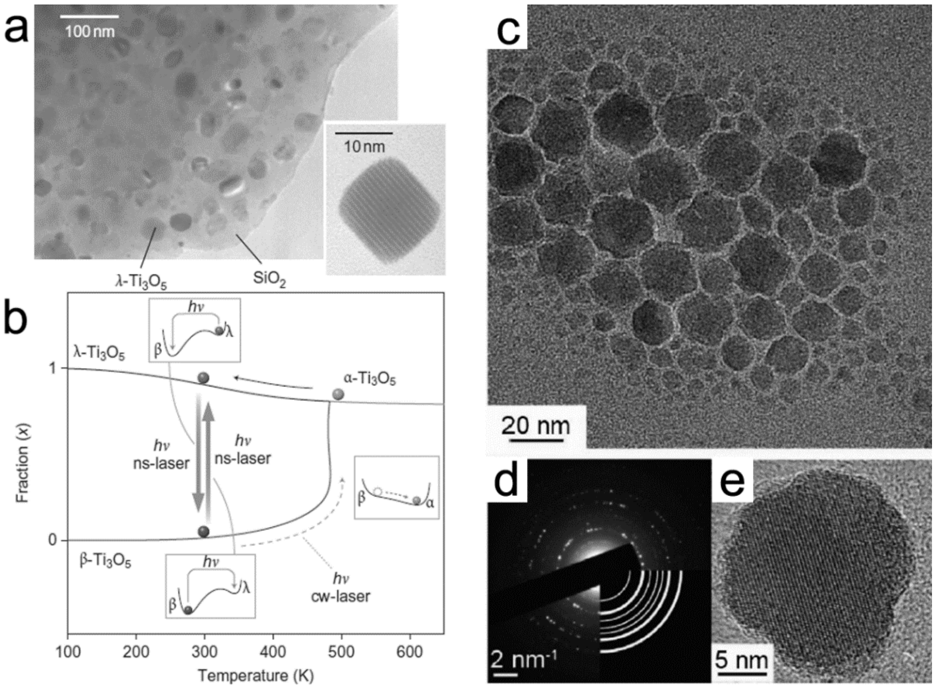

Figure 22. (a) TEM image of λ-Ti_3O_5 into a silica matrix. (b) photo-induced phase transition between λ-Ti_3O_5 and β-Ti_3O_5. (c) TEM image of bixbyite V_2O_3, corresponding (d) SAED pattern and (e) HRTEM image. Source: adapted from (a, b) Ohkoshi *et al.*[104] with permission of Springer, and (c-e) Bergerud *et al.*[161] with permission of American Chemical Society, Copyright 2013.

4.2.Beyond hard templating for isolating nanostructures of metastable oxides

Templating is not always mandatory to take benefit from the effect of the nanoscale if the growth of the nanostructures can be limited, even at high temperature. This has been demonstrated both on ε-Fe_2O_3 and λ–Ti_3O_5. ε-Fe_2O_3 nanowires and nanobelts could be obtained by pulsed laser deposition (PLD) through a vapor-liquid-solid mechanism catalyzed by gold nanoparticles, which restricts lateral growth of the wires.[156] Epitaxial growth of thin films ε-Fe_2O_3 over several substrates, especially $AlFeO_3$, has also been reported by PLD at ca. 800 °C.[162] Likewise, λ-Ti_3O_5 flakes made of 25 nm nanoparticles could also be obtained by treating 7 nm TiO_2 anatase at 1200 °C under hydrogen,[104] thus suggesting that anatase is the actual TiO_2 precursor of λ-Ti_3O_5, contrary to rutile for Magnéli phases. These experiments show that hard templating is not mandatory to isolate high temperature phases thanks to the nanoscale, as long as nanocrystal domains remain small enough to ensure that the crystallite surface contribution can still impact the overall energetics.

4.3. Colloidal syntheses

The structural transformations described above occur at high temperature. Other compounds can be formed at much lower temperature and thus do not require stringent templating or deposition strategies. This is the case of bixbyite V_2O_3 (**Figure 20c-e**), which was discovered recently by D. Milliron *et al.*[161] The authors used a colloidal synthesis to form 5 to 30 nm nanoparticles from vanadyl acetylacetonate in squalane with oleylamine and oleic acid at 310-370 °C. These nanoparticles are able to store reversibly oxygen in the interstitial sites of bixbyite in mild conditions.[163]

Concluding remarks

In this chapter, we have focused on multicationic oxides and/or oxides bearing metal oxidation states that are difficult to stabilize in solids and then that require specific synthetic conditions. These case-studies enable us to provide an overall survey of the synthesis strategies that have been and are currently developed to target such materials at the nanoscale. We have stressed out that, obviously, the choice of the synthesis conditions, including the temperature, the nature of the solvent, the use of a hard template must be driven by the compositional and structural features of the targeted materials and when possible, we have drawn some guidelines for choosing the right method, which we hope will be useful for the reader.

While this overview of course has not been exhaustive, let us stress out that, as detailed in the last section, some new oxides like ε–Fe_2O_3 and λ–Ti_2O_3 have been isolated only at the nanoscale, and sometimes with new crystal structures. To our knowledge, these new oxides have been first obtained by serendipity. Despite studies performed afterwards to identify the crossover particle size in which range these oxides can be isolated, it is striking that up to now, there is no possibility to predict the emergence of a new oxide when decreasing the particle size. This can be explained by the fact that the crossover size is often in the range of 10 nm, which represents a large number of atoms and then is extremely costly in terms of computation to enable tracing (composition, structure, size) maps. In view of this lack of exploration, it is likely that many new oxides are still to be discovered at the nanoscale. Because ε–Fe_2O_3, λ–Ti_2O_3 and bixbyite V_2O_3 are showing original properties with a potentially large societal impact, it appears of utmost importance to intensify efforts in exploring the role of nanoscaling for isolating new oxides.

References

1. Dadfar, S.M., Roemhild, K., Drude, N.I., von Stillfried, S., Knüchel, R., Kiessling, F., and Lammers, T. (2019) Iron oxide nanoparticles: Diagnostic, therapeutic and theranostic applications. *Adv. Drug Deliv. Rev.*, **138**, 302–325.

2. Védrine, J.C. (ed.) (2018) *Metal Oxides in Heterogeneous Catalysis*, Elsevier Inc., Amsterdam.

3. Sun, C., Alonso, J.A., and Bian, J. (2021) Recent Advances in Perovskite-Type Oxides for Energy Conversion and Storage Applications. **2000459**, 1–21.

4. Brahlek, M., Gupta, A. Sen, Lapano, J., Roth, J., Zhang, H., Zhang, L., Haislmaier, R., and Engel-herbert, R. (2018) Frontiers in the Growth of Complex Oxide Thin Films: Past , Present , and Future of Hybrid MBE. **1702772**, 1–41.

5. Stoerzinger, K.A., Risch, M., Suntivich, J., Lü, W.M., Zhou, J., Biegalski, M.D., Christen, H.M., Ariando, Venkatesan, T., and Shao-Horn, Y. (2013) Oxygen electrocatalysis on (001)-oriented manganese perovskite films: Mn valency and charge transfer at the nanoscale. *Energy {&} Environ. Sci.*, **6** (5), 1582.

6. Lee, D., Grimaud, A., Crumlin, E.J., Mezghani, K., Habib, M. a, Feng, Z., Hong, W.T., Biegalski, M.D., Christen, H.M., and Shao-horn, Y. (2013) Strain Influence on the Oxygen Electrocatalysis of the (100)-Oriented Epitaxial $La_2NiO_{4+\delta}$ Thin Films at Elevated Temperatures. *J. Phys. Chem. C*, **117** (100), 18789–18795.

7. Lee, D., Lee, Y.-L., Grimaud, A., Hong, W.T., Biegalski, M.D., Morgan, D., and Shao-Horn, Y. (2014) Strontium influence on the oxygen electrocatalysis of $La_{2-x}Sr_xNiO_{4\pm\delta}$ $(0.0 \leq x_{Sr} \leq 1.0)$ thin films. *J. Mater. Chem. A*, **2** (18), 6480.

8. Lee, J., Murugavel, P., Ryu, H., Lee, D., Jo, J.Y., Kim, J.W., Kim, H.J., Kim, K.H., Jo, Y., and Jung, M. (2006) Epitaxial stabilization of a new multiferroic hexagonal phase of $TbMnO_3$ thin films. *Adv. Mater.*, **18** (23), 3125–3129.

9. Li, Y., Weng, Y., Yin, X., Yu, X., Kumar, S.R.S., Wehbe, N., Wu, H., Alshareef, H.N., Pennycook, S.J., Breese, M.B.H., Chen, J., Dong, S., and Wu, T. (2018) Orthorhombic Ti_2O_3: A Polymorph-Dependent Narrow-Bandgap Ferromagnetic Oxide. *Adv. Funct. Mater.*, **28** (7), 1705657.

10. Li, Y., Yu, Z.G., Wang, L., Weng, Y., Tang, C.S., Yin, X., Han, K., Wu, H., Yu, X., Wong, L.M., Wan, D., Wang, X.R., Chai, J., Zhang, Y.W., Wang, S., Wang, J., Wee, A.T.S., Breese, M.B.H., Pennycook, S.J., Venkatesan, T., Dong, S., Xue, J.M., and Chen, J. (2019) Electronic-reconstruction-enhanced hydrogen evolution catalysis in oxide polymorphs. *Nat. Commun.*, **10** (1), 1–11.

11. Agrawal, A., Cho, S.H., Zandi, O., Ghosh, S., Johns, R.W., and Milliron, D.J. (2018) Localized Surface Plasmon Resonance in Semiconductor Nanocrystals. *Chem. Rev.*, **118** (6), 3121–3207.

12. Sanchez, C., Boissiere, C., Cassaignon, S., Chaneac, C., Durupthy, O., Faustini, M., Grosso, D., Laberty-Robert, C., Nicole, L., Portehault, D., Ribot, F., Rozes, L., and Sassoye, C. (2014) Molecular Engineering or Functional Inorganic and Hybrid Materials. *Chem. Mater.*, **26**, 221–238.

13. Centi, G., and Perathoner, S. (2008) Catalysis by layered materials: A review. *Microporous Mesoporous Mater.*, **107** (1–2), 3–15.

14. Han, M.H., Gonzalo, E., Singh, G., and Rojo, T. (2015) A comprehensive review of sodium layered oxides: powerful cathodes for Na-ion batteries. *Energy Environ. Sci.*, **8** (1), 81–102.

15. Hall, D.S., Lockwood, D.J., Bock, C., and MacDougall, B.R. (2015) Nickel hydroxides and related materials: a review of their structures, synthesis and properties. *Proc. R. Soc. A Math. Phys. Eng. Sci.*, **471** (2174), 20140792.

16. Kamath, P.V., Dixit, M., Indira, L., Schkla, A.K., Kumar, V.G., and Nunichandraiah, N. (1994) Stabilized α-$Ni(OH)_2$ as Electrode Material for Alkaline Secondary Cells. *J. Electrochem. Soc.*, **141** (11), 2956.

17. Freitas, M.B.J.G. (2001) Nickel hydroxide powder for NiOOH/$Ni(OH)_2$ electrodes of the alkaline batteries. *J. Power Sources*, **93** (1–2), 163–173.

18. Gao, M., Sheng, W., Zhuang, Z., Fang, Q., Gu, S., Jiang, J., and Yan, Y. (2014) Efficient water oxidation using nanostructured α-nickel-hydroxide as an electrocatalyst. *J. Am. Chem. Soc.*, **136** (19), 7077–7084.

19. Trotochaud, L., Young, S.L., Ranney, J.K., and Boettcher, S.W. (2014) Nickel-Iron oxyhydroxide oxygen-evolution electrocatalysts: The role of intentional and incidental iron incorporation. *J. Am. Chem. Soc.*, **136** (18), 6744–6753.

20. Trotochaud, L., Ranney, J.K., Williams, K.N., and Boettcher, S.W. (2012) Solution-Cast Metal Oxide Thin Film Electrocatalysts for Oxygen Evolution. *J. Am. Chem. Soc.*, **134** (41), 17253–17261.

21. Dai, L., Chen, Z., Li, L., Yin, P., Liu, Z., and Zhang, H. (2020) Ultrathin Ni(0)-Embedded $Ni(OH)_2$ Heterostructured Nanosheets with Enhanced Electrochemical Overall Water Splitting. *Adv. Mater.*, **32** (8), 1906915.

22. Pan, J., Sun, Y., Wan, P., Wang, Z., and Liu, X. (2005) Synthesis, characterization and electrochemical performance of battery grade NiOOH. *Electrochem. commun.*, **7** (8), 857–862.

23. Oliva, P., Leonardi, J., Laurent, J.F., Delmas, C., Braconnier, J.J., Figlarz, M., Fievet, F., and Guibert, A. d. (1982) Review of the structure and the electrochemistry of nickel hydroxides and oxy-hydroxides. *J. Power Sources*, **8** (2), 229–255.

24. Wang, Y., Delahaye, E., Leuvrey, C., Leroux, F., Rabu, P., and Rogez, G. (2016) Efficient Microwave-Assisted Functionalization of the Aurivillius-Phase $Bi_2SrTa_2O_9$. *Inorg. Chem.*, **55** (8), 4039–4046.

25. Moreno, J.M., Navarro, I., Díaz, U., Primo, J., and Corma, A. (2016) Single-Layered Hybrid Materials Based on 1D Associated Metalorganic Nanoribbons for Controlled Release of Pheromones. *Angew. Chem. Int. Ed.*, **128** (37), 11192–11196.

26. Liu, Z., Ma, R., Osada, M., Takada, K., and Sasaki, T. (2005) Selective and Controlled Synthesis of α- and β-Cobalt Hydroxides in Highly Developed Hexagonal Platelets. *J. Am. Chem. Soc.*, **127** (40), 13869–13874.

27. Butel, M., Gautier, L., and Delmas, C. (1999) Cobalt oxyhydroxides obtained by “chimie douce” reactions: structure and electronic conductivity properties. *Solid State Ionics*, **122** (1–4), 271–284.

28. Bardé, F., Palacin, M.-R., Beaudoin, B., Delahaye-Vidal, A., and Tarascon, J.-M.

(2004) New Approaches for Synthesizing γ III-CoOOH by Soft Chemistry. *Chem. Mater.*, **16** (2), 299–306.

29. Yang, J., Liu, H., Martens, W.N., and Frost, R.L. (2010) Synthesis and Characterization of Cobalt Hydroxide, Cobalt Oxyhydroxide, and Cobalt Oxide Nanodiscs. *J. Phys. Chem. C*, **114** (1), 111–119.

30. Pralong, V., Delahaye-Vidal, A., Beaudoin, B., Gérand, B., and Tarascon, J.-M. (1999) Oxidation mechanism of cobalt hydroxide to cobalt oxyhydroxide. *J. Mater. Chem.*, **9** (4), 955–960.

31. Audemer, A., Delahaye, R., Farhi, R., Sac-Epée, N., and Tarascon, J.-M. (1997) Electrochemical and Raman Studies of Beta-Type Nickel Hydroxides $Ni_{1-x}Co_x(OH)_2$ Electrode Materials. *J. Electrochem. Soc.*, **144** (8), 2614–2620.

32. Wang, H.-Y., Hsu, Y.-Y., Chen, R., Chan, T.-S., Chen, H.M., and Liu, B. (2015) Ni 3+ -Induced Formation of Active NiOOH on the Spinel Ni-Co Oxide Surface for Efficient Oxygen Evolution Reaction. *Adv. Energy Mater.*, **5** (10), 1500091.

33. Nai, J., Yin, H., You, T., Zheng, L., Zhang, J., Wang, P., Jin, Z., Tian, Y., Liu, J., Tang, Z., and Guo, L. (2015) Efficient Electrocatalytic Water Oxidation by Using Amorphous Ni-Co Double Hydroxides Nanocages. *Adv. Energy Mater.*, **5** (10), 1401880.

34. Balram, A., Zhang, H., and Santhanagopalan, S. (2017) Enhanced Oxygen Evolution Reaction Electrocatalysis via Electrodeposited Amorphous α-Phase Nickel-Cobalt Hydroxide Nanodendrite Forests. *ACS Appl. Mater. Interfaces*, **9** (34), 28355–28365.

35. Ito, M., and Nagira, T. (2005) Effect of the Polymerized Complex Process on Doping Limit of Thermoelectric $Na_xCo_{1-y}M_yO_2$ (M=Mn, Ni). *Mater. Trans.*, **46** (7), 1456–1461.

36. Gayathri, N., Bharathi, A., Sastry, V.S., Sundar, C.S., and Hariharan, Y. (2006) Ground state changes induced by Ni substitution in Na_xCoO_2. *Solid State Commun.*, **138** (10–11), 489–493.

37. Azor, A., Ruiz-Gonzalez, M.L., Gonell, F., Laberty-Robert, C., Parras, M., Sanchez, C., Portehault, D., and González-Calbet, J.M. (2018) Nickel-Doped Sodium Cobaltite 2D Nanomaterials: Synthesis and Electrocatalytic Properties. *Chem. Mater.*, **30** (15), 4986–4994.

38. Besselink, R., Stawski, T.M., Castricum, H.L., Blank, D.H.A., and ten Elshof, J.E. (2010) Exfoliation and Restacking of Lepidocrocite-type Layered Titanates Studied by Small-Angle X-ray Scattering. *J. Phys. Chem. C*, **114** (49), 21281–21286.

39. Schaak, R.E., and Mallouk, T.E. (2000) Prying Apart Ruddlesden−Popper Phases: Exfoliation into Sheets and Nanotubes for Assembly of Perovskite Thin Films. *Chem. Mater.*, **12** (11), 3427–3434.

40. Omomo, Y., Sasaki, T., Wang, and Watanabe, M. (2003) Redoxable Nanosheet Crystallites of MnO_2 Derived via Delamination of a Layered Manganese Oxide. *J. Am. Chem. Soc.*, **125** (12), 3568–3575.

41. Ko, J.S., Doan-Nguyen, V.V.T., Kim, H.-S., Muller, G.A., Serino, A.C., Weiss, P.S., and Dunn, B.S. (2017) $Na_2Ti_3O_7$ Nanoplatelets and Nanosheets Derived from a Modified Exfoliation Process for Use as a High-Capacity Sodium-Ion Negative Electrode. *ACS Appl. Mater. Interfaces*, **9** (2), 1416–1425.

42. Sakai, N., Fukuda, K., Ma, R., and Sasaki, T. (2018) Synthesis and Substitution Chemistry of Redox-Active Manganese/Cobalt Oxide Nanosheets. *Chem. Mater.*, **30** (5), 1517–1523.

43. Acosta, M., Novak, N., Rojas, V., Patel, S., Vaish, R., Koruza, J., Rossetti, G.A., and Rödel, J. (2017) $BaTiO_3$ -based piezoelectrics: Fundamentals, current status, and perspectives. *Appl. Phys. Rev.*, **4** (4), 041305.

44. Jiang, B., Iocozzia, J., Zhao, L., Zhang, H., Harn, Y.-W., Chen, Y., and Lin, Z. (2019) Barium titanate at the nanoscale: controlled synthesis and dielectric and ferroelectric properties. *Chem. Soc. Rev.*, **48** (4), 1194–1228.

45. Modeshia, D.R., and Walton, R.I. (2010) Solvothermal synthesis of perovskites and pyrochlores: crystallisation of functional oxides under mild conditions. *Chem. Soc. Rev.*, **39** (11), 4303.

46. Hertl, W. (1988) Kinetics of Barium Titanate Synthesis. *J. Am. Ceram. Soc.*, **71** (10), 879–883.

47. Eckert Jr., J.O., Hung-Houston, C.C., Gersten, B.L., Lencka, M.M., and Riman, R.E. (1996) Kinetic and Mechanism of Hydrothermal of Barium Titanate. *J. Am. Ceram. Soc.*, **79** (11), 2929–2939.

48. Yang, J., Zhang, J., Liang, C., Wang, M., Zhao, P., Liu, M., Liu, J., and Che, R. (2013) Ultrathin $BaTiO_3$ Nanowires with High Aspect Ratio: A Simple One-Step Hydrothermal Synthesis and Their Strong Microwave Absorption. *ACS Appl. Mater. Interfaces*, **5** (15), 7146–7151.

49. Zhu, Y.-F., Zhang, L., Natsuki, T., Fu, Y.-Q., and Ni, Q.-Q. (2012) Facile Synthesis of $BaTiO_3$ Nanotubes and Their Microwave Absorption Properties. *ACS Appl. Mater. Interfaces*, **4** (4), 2101–2106.

50. O'Brien, S., Brus, L., and Murray, C.B. (2001) Synthesis of Monodisperse Nanoparticles of Barium Titanate: Toward a Generalized Strategy of Oxide Nanoparticle Synthesis. *J. Am. Chem. Soc.*, **123** (48), 12085–12086.

51. Urban, J.J., Yun, W.S., Gu, Q., and Park, H. (2002) Synthesis of Single-Crystalline Perovskite Nanorods Composed of Barium Titanate and Strontium Titanate. *J. Am. Chem. Soc.*, **124** (7), 1186–1187.

52. Adireddy, S., Lin, C., Cao, B., Zhou, W., and Caruntu, G. (2010) Solution-Based Growth of Monodisperse Cube-Like $BaTiO_3$ Colloidal Nanocrystals. *Chem. Mater.*, **22** (6), 1946–1948.

53. Niederberger, M., Pinna, N., Polleux, J., and Antonietti, M. (2004) A General Soft-Chemistry Route to Perovskites and Related Materials: Synthesis of BaTiO3, BaZrO3, and $LiNbO_3$ Nanoparticles. *Angew. Chemie Int. Ed.*, **43** (17), 2270–2273.

54. Niederberger, M., Garnweitner, G., Pinna, N., and Antonietti, M. (2004) Nonaqueous and Halide-Free Route to Crystalline $BaTiO_3$, $SrTiO_3$, and $(Ba,Sr)TiO_3$ Nanoparticles via a Mechanism Involving C−C Bond Formation. *J. Am. Chem. Soc.*, **126** (29), 9120–9126.

55. Mao, Y., Banerjee, S., and Wong, S.S. (2003) Large-Scale Synthesis of Single-Crystalline Perovskite Nanostructures. *J. Am. Chem. Soc.*, **125** (51), 15718–15719.

56. Deng, H., Qiu, Y., and Yang, S. (2009) General surfactant-free synthesis of $MTiO_3$ (M = Ba, Sr, Pb) perovskite nanostrips. *J. Mater. Chem.*, **19** (7), 976.

57. Huang, K.-C., Huang, T.-C., and Hsieh, W.-F. (2009) Morphology-Controlled Synthesis of Barium Titanate Nanostructures. *Inorg. Chem.*, **48** (19), 9180–9184.

58. Fu, J., Hou, Y., Zheng, M., Wei, Q., Zhu, M., and Yan, H. (2015) Improving Dielectric Properties of PVDF Composites by Employing Surface Modified Strong Polarized $BaTiO_3$ Particles Derived by Molten Salt Method. *ACS Appl. Mater. Interfaces*, **7** (44), 24480–24491.

59. Liu, H., Hu, C., and Wang, Z.L. (2006) Composite-Hydroxide-Mediated Approach for the Synthesis of Nanostructures of Complex Functional-Oxides. *Nano Lett.*, **6** (7), 1535–1540.

60. Dutta, D.P., Mandal, B.P., Naik, R., Lawes, G., and Tyagi, A.K. (2013) Magnetic, Ferroelectric, and Magnetocapacitive Properties of Sonochemically Synthesized Sc-Doped $BiFeO_3$ Nanoparticles. *J. Phys. Chem. C*, **117** (5), 2382–2389.

61. Park, T.J., Papaefthymiou, G.C., Viescas, A.J., Moodenbaugh, A.R., and Wong, S.S. (2007) Size-dependent magnetic properties of single-crystalline multiferroic $BiFeO_3$ nanoparticles. *Nano Lett.*, **7** (3), 766–772.

62. Selbach, S.M., Tybell, T., Einarsrud, M.A., and Grande, T. (2007) Size-dependent properties of multiferroic $BiFeO_3$ nanoparticles. *Chem. Mater.*, **19** (26), 6478–6484.

63. Ghosh, S., Dasgupta, S., Sen, A., and Sekhar Maiti, H. (2005) Low-Temperature Synthesis of Nanosized Bismuth Ferrite by Soft Chemical Route. *J. Am. Ceram. Soc.*, **88** (5), 1349–1352.

64. Han, J.-T., Huang, Y.-H., Wu, X.-J., Wu, C.-L., Wei, W., Peng, B., Huang, W., and Goodenough, J.B. (2006) Tunable Synthesis of Bismuth Ferrites with Various Morphologies. *Adv. Mater.*, **18** (16), 2145–2148.

65. Wang, Y., Xu, G., Yang, L., Ren, Z., Wei, X., Weng, W., Du, P., Shen, G., and Han, G. (2007) Alkali Metal Ions-Assisted Controllable Synthesis of Bismuth Ferrites by a Hydrothermal Method. *J. Am. Ceram. Soc.*, **90** (11), 3673–3675.

66. Wang, Y., Xu, G., Ren, Z., Wei, X., Weng, W., Du, P., Shen, G., and Han, G. (2007) Mineralizer-Assisted Hydrothermal Synthesis and Characterization of $BiFeO_3$ Nanoparticles. *J. Am. Ceram. Soc.*, **90** (8), 2615–2617.

67. Joshi, U.A., Jang, J.S., Borse, P.H., and Lee, J.S. (2008) Microwave synthesis of single-crystalline perovskite $BiFeO_3$ nanocubes for photoelectrode and photocatalytic applications. *Appl. Phys. Lett.*, **92** (24), 242106.

68. Chen, J., Xing, X., Watson, A., Wang, W., Yu, R., Deng, J., Yan, L., Sun, C., and Chen, X. (2007) Rapid Synthesis of Multiferroic $BiFeO_3$ Single-Crystalline Nanostructures. *Chem. Mater.*, **19** (15), 3598–3600.

69. He, X., and Gao, L. (2009) Synthesis of pure phase $BiFeO_3$ powders in molten alkali metal nitrates. *Ceram. Int.*, **35** (3), 975–978.

70. el Hadri, A., Gómez-Recio, I., del Río, E., Hernández-Garrido, J.C., Cortés-Gil, R., Hernando, M., Varela, Á., Gutiérrez-Alonso, Á., Parras, M., Delgado, J.J., Pérez-Omil, J.A., Blanco, G., Calvino, J.J., and González-Calbet, J.M. (2017) Critical Influence of

Redox Pretreatments on the CO Oxidation Activity of $BaFeO_{3-\delta}$ Perovskites: An in-Depth Atomic-Scale Analysis by Aberration-Corrected and in Situ Diffraction Techniques. *ACS Catal.*, **7**, 8653–8663.

71. Stoerzinger, K.A., Lü, W., Li, C., Ariando, Venkatesan, T., and Shao-Horn, Y. (2015) Highly Active Epitaxial $La_{(1-x)}Sr_xMnO_3$ Surfaces for the Oxygen Reduction Reaction: Role of Charge Transfer. *J. Phys. Chem. Lett.*, **6** (8), 1435–1440.

72. Gonell, F., Sanchez-Sanchez, C.M., Vivier, V., Méthivier, C., Laberty-Robert, C., and Portehault, D. (2020) Structure-activity relationship in manganese perovskite oxide nanocrystals from molten salts for efficient oxygen reduction reaction electrocatalysis. *Chem. Mater.*, **32**, 4241-4247.

73. Thi N'Goc, H. Le, Mouafo, L.D.N., Etrillard, C., Torres-Pardo, A., Dayen, J.-F., Rano, S., Rousse, G., Laberty-Robert, C., Calbet, J.G., Drillon, M., Sanchez, C., Doudin, B., and Portehault, D. (2017) Surface-Driven Magnetotransport in Perovskite Nanocrystals. *Adv. Mater.*, **29** (9), 1604745.

74. Vázquez-Vázquez, C., and Arturo López-Quintela, M. (2006) Solvothermal synthesis and characterisation of $La_{1-x}A_xMnO_3$ nanoparticles. *J. Solid State Chem.*, **179** (10), 3229–3237.

75. Hou, L., Zhang, H., Dong, L., Zhang, L., Duprez, D., and Royer, S. (2017) A simple non-aqueous route to nano-perovskite mixed oxides with improved catalytic properties. *Catal. Today*, **287**, 30–36.

76. Portehault, D., Cassaignon, S., Baudrin, E., and Jolivet, J.-P. (2008) Design of Hierarchical Core−Corona Architectures of Layered Manganese Oxides by Aqueous Precipitation. *Chem. Mater.*, **20** (19), 6140–6147.

77. Spooren, J., and Walton, R.I. (2005) Hydrothermal synthesis of the perovskite manganites $Pr_{0.5}Sr_{0.5}MnO_3$ and $Nd_{0.5}Sr_{0.5}MnO_3$ and alkali-earth manganese oxides $CaMn_2O_4$, 4H-$SrMnO_3$, and 2H-$BaMnO_3$. *J. Solid State Chem.*, **178** (5), 1683–1691.

78. Shimizu, Y., and Murata, T. (2005) Sol-Gel Synthesis of Perovskite-Type Lanthanum Manganite Thin Films and Fine Powders Using Metal Acetylacetonate and Poly(vinyl alcohol). *J. Am. Ceram. Soc.*, **80** (10), 2702–2704.

79. Lin, H., Liu, P., Wang, S., Zhang, Z., Dai, Z., Tan, S., and Chen, D. (2019) A highly efficient electrocatalyst for oxygen reduction reaction: Three-dimensionally ordered macroporous perovskite $LaMnO_3$. *J. Power Sources*, **412**, 701–709.

80. Bell, R. (2000) Influence of synthesis route on the catalytic properties of $La_{1-x}Sr_xMnO_3$. *Solid State Ionics*, **131** (3–4), 211–220.

81. Taguchi, H., Matsuda, D., Nagao, M., Tanihata, K., and Miyamoto, Y. (1992) Synthesis of Perovskite-Type $(La_{1-x}Sr_x)MnO_3$ (0 X 0.3) at Low Temperature. *J. Am. Ceram. Soc.*, **75** (1), 201–202.

82. Cai, B., Akkiraju, K., Mounfield, W.P., Wang, Z., Li, X., Huang, B., Yuan, S., Su, D., Román-Leshkov, Y., and Shao-Horn, Y. (2019) Solid-State Gelation for Nanostructured Perovskite Oxide Aerogels. *Chem. Mater.*, **31** (22), 9422–9429.

83. Gonell, F., Alem, N., Dunne, P., Crochet, G., Beaunier, P., Méthivier, C., Montero, D., Laberty-Robert, C., Doudin, B., and Portehault, D. (2019) Versatile Molten Salt Synthesis of Manganite Perovskite Oxide Nanocrystals and Their Magnetic Properties.

ChemNanoMat, **5** (3), 358–363.

84. Gonell, F., Sánchez-Sánchez, C.M., Vivier, V., Laberty-Robert, C., and Portehault, D. (2020) Experimental Descriptors for the Synthesis of Multicationic Nickel Perovskite Nanoparticles for Oxygen Reduction. *ACS Appl. Nano Mater.*, **3** (8), 7482–7489.

85. Chen, X., Liu, L., and Huang, F. (2015) Black titanium dioxide (TiO_2) nanomaterials. *Chem. Soc. Rev.*, **44** (7), 1861–1885.

86. Tominaka, S., Tsujimoto, Y., Matsushita, Y., and Yamaura, K. (2011) Synthesis of Nanostructured Reduced Titanium Oxide: Crystal Structure Transformation Maintaining Nanomorphology. *Angew. Chem. Int. Ed.*, **50** (32), 7418–7421.

87. Jing, Y., Almassi, S., Mehraeen, S., LeSuer, R.J., and Chaplin, B.P. (2018) The roles of oxygen vacancies, electrolyte composition, lattice structure, and doping density on the electrochemical reactivity of Magnéli phase TiO_2 anodes. *J. Mater. Chem. A*, **6** (46), 23828–23839.

88. Pan, Y., Li, Y.Q., Zheng, Q.H., and Xu, Y. (2019) Point defect of titanium sesquioxide Ti_2O_3 as the application of next generation Li-ion batteries. *J. Alloys Compd.*, **786**, 621–626.

89. Chen, D., Chen, C., Baiyee, Z.M., Shao, Z., and Ciucci, F. (2015) Nonstoichiometric Oxides as Low-Cost and Highly-Efficient Oxygen Reduction/Evolution Catalysts for Low-Temperature Electrochemical Devices. *Chem. Rev.*, **115** (18), 9869–9921.

90. Wang, J., Li, Y., Deng, L., Wei, N., Weng, Y., Dong, S., Qi, D., Qiu, J., Chen, X., and Wu, T. (2017) High-Performance Photothermal Conversion of Narrow-Bandgap Ti_2O_3 Nanoparticles. *Adv. Mater.*, **29** (3), 1603730.

91. Mercier, J., and Lakkis, S. (1973) Preparation of titanium lower oxides single crystals by chemical transport reaction. *J. Cryst. Growth*, **20** (3), 195–201.

92. Strobel, P., and Le Page, Y. (1982) Crystal growth of Ti_nO_{2n-1} oxides(n=2 to 9). *J. Mater. Sci.*, **17** (8), 2424–2430.

93. Kobayashi, Y., Hernandez, O.J., Sakaguchi, T., Yajima, T., Roisnel, T., Tsujimoto, Y., Morita, M., Noda, Y., Mogami, Y., Kitada, A., Ohkura, M., Hosokawa, S., Li, Z., Hayashi, K., Kusano, Y., Kim, J. eun, Tsuji, N., Fujiwara, A., Matsushita, Y., Yoshimura, K., Takegoshi, K., Inoue, M., Takano, M., and Kageyama, H. (2012) An oxyhydride of $BaTiO_3$ exhibiting hydride exchange and electronic conductivity. *Nat. Mater.*, **11** (6), 507–511.

94. Andersson, S., Collen, B., Kuylenstierna, U., and Magneli, A. (1957) Phase Analysis Studies on the Titanium-Oxygen System. *Acta Chem. Scand.*, **11**, 1641–1652.

95. Andersson, G. (1954) Studies on Vanadium Oxides. *Acta Chem. Scand.*, **8**, 1599–1606.

96. Magneli, A. (1948) The Crystal Structures of Mo_9O_{26} (beta-Molybdenum Oxide) and Mo_8O_{23} (beta-Molybdenum Oxide). *Acta Chem. Scand.*, **2**, 501–517.

97. Migas, D.B., Shaposhnikov, V.L., and Borisenko, V.E. (2010) Tungsten oxides. II. The metallic nature of Magnéli phases. **108** (9), 93714.

98. Xu, B., Sohn, H.Y., Mohassab, Y., and Lan, Y. (2016) Structures, preparation and applications of titanium suboxides. *RSC Adv.*, **6** (83), 79706–79722.

99. Yoshimatsu, K., Sakata, O., and Ohtomo, A. (2017) Superconductivity in Ti4O7 and γ-Ti_3O_5 films. *Sci. Rep.*, **7** (1), 12544.

100. Åsbrink, S., and Magnéli, A. (1959) Crystal structure studies on trititanium pentoxide, Ti_3O_5. *Acta Crystallogr.*, **12** (8), 575–581.

101. Åsbrink, G., Åsbrink, S., Magnéli, A., Okinaka, H., Kosuge, K., and Kachi, S. (1971) A Ti_3O_5 Modification of V_3O_5-type Structure. *Acta Chem. Scand.*, **25**, 3889–3890.

102. Hong, S.-H.; Åsbrink, S. The Structure of γ-Ti_3O_5 at 297 K. Acta Crystallogr. Sect. B 1982, 38 (10), 2570–2576. https://doi.org/10.1107/S056774088200939X. *Acta Crystallogr. Sect. B*, **38** (10), 2570–2576.

103. Tanaka, K., Nasu, T., Miyamoto, Y., Ozaki, N., Tanaka, S., Nagata, T., Hakoe, F., Yoshikiyo, M., Nakagawa, K., Umeta, Y., Imoto, K., Tokoro, H., Namai, A., and Ohkoshi, S. (2015) Structural Phase Transition between γ-Ti_3O_5 and δ-Ti_3O_5 by Breaking of a One-Dimensionally Conducting Pathway. *Cryst. Growth Des.*, **15** (2), 653–657.

104. Ohkoshi, S., Tsunobuchi, Y., Matsuda, T., Hashimoto, K., Namai, A., Hakoe, F., and Tokoro, H. (2010) Synthesis of a metal oxide with a room-temperature photoreversible phase transition. *Nat. Chem.*, **2** (7), 539–545.

105. Chen, X., Liu, L., Yu, P.Y., and Mao, S.S. (2011) Increasing solar absorption for photocatalysis with black hydrogenated titanium dioxide nanocrystals. *Science*, **331** (6018), 746–750.

106. Tominaka, S., Yoshikawa, H., Matsushita, Y., and Cheetham, A.K. (2014) Topotactic reduction of oxide nanomaterials: unique structure and electronic properties of reduced TiO_2 nanoparticles. *Mater. Horizons*, **1** (1), 106–110.

107. Zeng, P., Chen, M., Jiang, S., Li, Y., Xie, X., Liu, H., Hu, X., Wu, C., Shu, H., and Wang, X. (2019) Architecture and Performance of the Novel Sulfur Host Material Based on Ti_2O_3 Microspheres for Lithium–Sulfur Batteries. *ACS Appl. Mater. Interfaces*, **11** (25), 22439–22448.

108. Tominaka, S. (2012) Facile synthesis of nanostructured reduced titanium oxides using borohydride toward the creation of oxide-based fuel cell electrodes. *Chem. Commun.*, **48** (64), 7949–7951.

109. Kuroda, Y., Igarashi, H., Nagai, T., Napporn, T.W., Matsuzawa, K., Mitsushima, S., Ota, K., and Ishihara, A. (2019) Templated Synthesis of Carbon-Free Mesoporous Magnéli-Phase Titanium Suboxide. *Electrocatalysis*, **10** (5), 459–465.

110. Portehault, D., Maneeratana, V., Candolfi, C., Oeschler, N., Veremchuk, I., Grin, Y., Sanchez, C., and Antonietti, M. (2011) Facile General Route toward Tunable Magnéli Nanostructures and Their Use As Thermoelectric Metal Oxide/Carbon Nanocomposites. *ACS Nano*, **5** (11), 9052–9061.

111. Harada, S., Tanaka, K., and Inui, H. (2010) Thermoelectric properties and crystallographic shear structures in titanium oxides of the Magnèli phases. *J. Appl. Phys.*, **108** (8), 83703.

112. Lu, Y., Matsuda, Y., Sagara, K., Hao, L., Otomitsu, T., and Yoshida, H. (2011) Fabrication and Thermoelectric Properties of Magneli Phases by Adding Ti into TiO_2. *Adv. Mater. Res.*, **415–417**, 1291–1296.

113. Fan, Y., Feng, X., Zhou, W., Murakami, S., Kikuchi, K., Nomura, N., Wang, L., Jiang, W., and Kawasaki, A. (2018) Preparation of monophasic titanium sub-oxides of Magnéli phase with enhanced thermoelectric performance. *J. Eur. Ceram. Soc.*, **38** (2), 507–513.

114. Cao, X., Sun, Z., Zheng, X., Tian, J., Jin, C., Yang, R., Li, F., He, P., and Zhou, H. (2017) $MnCo_2O_4$ decorated Magnéli phase titanium oxide as a carbon-free cathode for Li–O_2 batteries. *J. Mater. Chem. A*, **5** (37), 19991–19996.

115. Ma, M., You, S., Liu, G., Qu, J., and Ren, N. (2016) Macroporous monolithic Magnéli-phase titanium suboxides as anode material for effective bioelectricity generation in microbial fuel cells. *J. Mater. Chem. A*, **4** (46), 18002–18007.

116. Tao, X., Wang, J., Ying, Z., Cai, Q., Zheng, G., Gan, Y., Huang, H., Xia, Y., Liang, C., Zhang, W., and Cui, Y. (2014) Strong Sulfur Binding with Conducting Magnéli-Phase Ti_nO_{2n-1} Nanomaterials for Improving Lithium–Sulfur Batteries. *Nano Lett.*, **14** (9), 5288–5294.

117. Mei, S., Jafta, C.J., Lauermann, I., Ran, Q., Kärgell, M., Ballauff, M., and Lu, Y. (2017) Porous Ti_4O_7 Particles with Interconnected-Pore Structure as a High-Efficiency Polysulfide Mediator for Lithium–Sulfur Batteries. *Adv. Funct. Mater.*, **27** (26), 1701176.

118. Baktash, E., Capitolis, J., Tinat, L., Larquet, C., Chan Chang, T.H.C., Gallet, J.-J., Bournel, F., Sanchez, C., Carenco, S., and Portehault, D. (2019) Different Reactivity of Rutile and Anatase TiO_2 Nanoparticles: Synthesis and Surface States of Nanoparticles of Mixed-Valence Magnéli Oxides. *Chem. a Eur. J.*, **25** (47), 11114–11120.

119. Wei, H., Rodriguez, E.F., Best, A.S., Hollenkamp, A.F., Chen, D., and Caruso, R.A. (2017) Chemical Bonding and Physical Trapping of Sulfur in Mesoporous Magnéli Ti_4O_7 Microspheres for High-Performance Li–S Battery. *Adv. Energy Mater.*, **7** (4), 1601616.

120. Wang, G., Liu, Y., Ye, J., Lin, Z., and Yang, X. (2020) Electrochemical oxidation of methyl orange by a Magnéli phase Ti_4O_7 anode. *Chemosphere*, **241**, 125084.

121. Huang, S.-S., Lin, Y.-H., Chuang, W., Shao, P.-S., Chuang, C.-H., Lee, J.-F., Lu, M.-L., Weng, Y.-T., and Wu, N.-L. (2018) Synthesis of High-Performance Titanium Sub-Oxides for Electrochemical Applications Using Combination of Sol–Gel and Vacuum-Carbothermic Processes. *ACS Sustain. Chem. Eng.*, **6** (3), 3162–3168.

122. Sanchez, C., Belleville, P., Popall, M., and Nicole, L. (2011) Applications of advanced hybrid organic–inorganic nanomaterials: from laboratory to market. *Chem. Soc. Rev.*, **40**, 696–753.

123. Portehault, D., Delacroix, S., Gouget, G., Grosjean, R., and Chan-Chang, T.-H.-C. (2018) Beyond the Compositional Threshold of Nanoparticle-Based Materials. *Acc. Chem. Res.*, **51** (4), 930–939.

124. Pang, Q., Kundu, D., Cuisinier, M., and Nazar, L.F. (2014) Surface-enhanced redox chemistry of polysulphides on a metallic and polar host for lithium-sulphur batteries. *Nat. Commun.*, **5** (1), 4759.

125. Lee, Y.-J., Lee, T., and Soon, A. (2019) Phase Stability Diagrams of Group 6 Magnéli Oxides and Their Implications for Photon-Assisted Applications. *Chem. Mater.*, **31**

(11), 4282–4290.

126. Cheng, W., Ju, Y., Payamyar, P., Primc, D., Rao, J., Willa, C., Koziej, D., and Niederberger, M. (2015) Large-Area Alignment of Tungsten Oxide Nanowires over Flat and Patterned Substrates for Room-Temperature Gas Sensing. *Angew. Chem. Int. Ed.*, **54** (1), 340–344.

127. Polleux, J., Pinna, N., Antonietti, M., and Niederberger, M. (2005) Growth and assembly of crystalline tungsten oxide nanostructures assisted by bioligation. *J. Am. Chem. Soc.*, **127** (44), 15595–601.

128. Deshmukh, R., and Niederberger, M. (2017) Mechanistic Aspects in the Formation, Growth and Surface Functionalization of Metal Oxide Nanoparticles in Organic Solvents. *Chem. Eur. J.,* **23** (36), 8542-8570.

129. Zhang, W., Fan, Y., Yuan, T., Lu, B., Liu, Y., Li, Z., Li, G., Cheng, Z., and Xu, J. (2020) Ultrafine Tungsten Oxide Nanowires: Synthesis and Highly Selective Acetone Sensing and Mechanism Analysis. *ACS Appl. Mater. Interfaces*, **12** (3), 3755–3763.

130. Mattox, T.M., Bergerud, A., Agrawal, A., and Milliron, D.J. (2014) Influence of Shape on the Surface Plasmon Resonance of Tungsten Bronze Nanocrystals. *Chem. Mater.*, **26** (5), 1779–1784.

131. Zhou, Y., Li, N., Xin, Y., Cao, X., Ji, S., and Jin, P. (2017) Cs_xWO_3 nanoparticle-based organic polymer transparent foils: low haze, high near infrared-shielding ability and excellent photochromic stability. *J. Mater. Chem. C*, **5** (25), 6251–6258.

132. Runnerstrom, E.L., Llordés, A., Lounis, S.D., and Milliron, D.J. (2014) Nanostructured electrochromic smart windows: traditional materials and NIR-selective plasmonic nanocrystals. *Chem. Commun.*, **50** (73), 10555–10572.

133. Migas, D.B., Shaposhnikov, V.L., Rodin, V.N., and Borisenko, V.E. (2010) Tungsten oxides. I. Effects of oxygen vacancies and doping on electronic and optical properties of different phases of WO_3. *J. Appl. Phys.,* **108** (9), 93713.

134. Kim, J., Agrawal, A., Krieg, F., Bergerud, A., and Milliron, D.J. (2016) The Interplay of Shape and Crystalline Anisotropies in Plasmonic Semiconductor Nanocrystals. *Nano Lett.*, **16** (6), 3879–3884.

135. Masuda, T., and Yao, H. (2020) Intense Plasmon-Induced Magneto-Optical Activity in Substoichiometric Tungsten Oxide (WO_{3-x}) Nanowires/Nanorods. *J. Phys. Chem. C*, **124** (28), 15460–15467.

136. Manthiram, K., and Alivisatos, A.P. (2012) Tunable Localized Surface Plasmon Resonances in Tungsten Oxide Nanocrystals. *J. Am. Chem. Soc.*, **134** (9), 3995–3998.

137. Shi, S., Xue, X., Feng, P., Liu, Y., Zhao, H., and Wang, T. (2008) Low-temperature synthesis and electrical transport properties of $W_{18}O_{49}$ nanowires. *J. Cryst. Growth*, **310** (2), 462–466.

138. Besnardiere, J., Ma, B., Torres-Pardo, A., Wallez, G., Kabbour, H., González-Calbet, J.M., Von Bardeleben, H.J., Fleury, B., Buissette, V., Sanchez, C., Le Mercier, T., Cassaignon, S., and Portehault, D. (2019) Structure and electrochromism of two-dimensional octahedral molecular sieve h'-WO_3. *Nat. Commun.*, **10** (1), 327.

139. Ranade, M.R., Navrotsky, A., Zhang, H.Z., Banfield, J.F., Elder, S.H., Zaban, A.,

Borse, P.H., Kulkarni, S.K., Doran, G.S., and Whitfield, H.J. (2002) Energetics of nanocrystalline TiO_2. *Proc. Natl. Acad. Sci. U. S. A.*, **99**, 6476–6481.

140. Levchenko, A.A., Li, G., Boerio-Goates, J., Woodfield, B.F., and Navrotsky, A. (2006) TiO_2 stability landscape: Polymorphism, surface energy, and bound water energetics. *Chem. Mater.*, **18** (26), 6324–6332.

141. Navrotsky, A. (2004) Energetic clues to pathways to biomineralization: precursors, clusters, and nanoparticles. *Proc. Natl. Acad. Sci. U. S. A.*, **101** (33), 12096–101.

142. Forestier, H., and Guiot-Guillain, G. (1934) Une nouvelle varieté ferromagnétique de sesquioxide de fer. *Compte rendu l'Académie des Sci.*, **199**, 720.

143. Schrader, R., and Büttner, G. (1963) Eine neue Eisen (III)-oxidphase: ε-Fe_2O_3. *Zeitschrift für Anorg. und Allg. Chemie*, **320** (5-6), 220–234.

144. Walter-Lévy, L., and Quémeneu, E. (1963) Chimie minerale-sur la therolyse du sulfate ferrique basique $6Fe_2(SO_4)_3$, Fe_2O_3,nH_2O. *Comptes rendus l'academie des Sci.*, **257** (22), 3410.

145. Tronc, E., Chanéac, C., and Jolivet, J.P. (1998) Structural and Magnetic Characterization of ε-Fe_2O_3. *J. Solid State Chem.*, **139** (139), 93–104.

146. Jin, J., Ohkoshi, S.I., and Hashimoto, K. (2004) Giant Coercive Field of Nanometer-Sized Iron Oxide. *Adv. Mater.*, **16** (1), 48–51.

147. Popovici, M., Gich, M., Nižňanský, D., Roig, A., Savii, C., Casas, L., Molins, E., Zaveta, K., Enache, C., and Sort, J. (2004) Optimized synthesis of the elusive ε-Fe_2O_3 phase via sol-gel chemistry. *Chem. Mater.*, **16** (25), 5542–5548.

148. Ohkoshi, S.I., Kuroki, S., Sakurai, S., Matsumoto, K., Sato, K., and Sasaki, S. (2007) A millimeter-wave absorber based on gallium-substituted ε-iron oxide nanomagnets. *Angew. Chem. Int. Ed.*, **46** (44), 8392–8395.

149. Guan, X., Yao, L., Rushchanskii, K.Z., Inkinen, S., Yu, R., Ležaić, M., Sánchez, F., Gich, M., and van Dijken, S. (2020) Unconventional Ferroelectric Switching via Local Domain Wall Motion in Multiferroic ε-Fe_2O_3 Films. *Adv. Electron. Mater.*, **6** (4).

150. Ohkoshi, S., Imoto, K., Namai, A., Yoshikiyo, M., Miyashita, S., Qiu, H., Kimoto, S., Kato, K., and Nakajima, M. (2019) Rapid Faraday Rotation on ε-Iron Oxide Magnetic Nanoparticles by Visible and Terahertz Pulsed Light. *J. Am. Chem. Soc.*, **141** (4), 1775–1780.

151. Taboada, E., Gich, M., and Roig, A. (2009) Nanospheres of silica with an ε-Fe_2O_3 single crystal nucleus. *ACS Nano*, **3** (11), 3377–3382.

152. Tuček, J., Zbořil, R., Namai, A., and Ohkoshi, S.I. (2010) ε-Fe_2O_3: An advanced nanomaterial exhibiting giant coercive field, millimeter-wave ferromagnetic resonance, and magnetoelectric coupling. *Chem. Mater.*, **22** (24), 6483–6505.

153. Sakurai, S., Namai, A., Hashimoto, K., and Ohkoshi, S.I. (2009) First observation of phase transformation of all four Fe_2O_3 phases ($\gamma \rightarrow \varepsilon \rightarrow \beta \rightarrow \alpha$-phase). *J. Am. Chem. Soc.*, **131** (51), 18299–18303.

154. Gich, M., Frontera, C., Roig, A., Fontcuberta, J., Molins, E., Bellido, N., Simon, C., and Fleta, C. (2006) Magnetoelectric coupling in ε-Fe_2O_3 nanoparticles. *Nanotechnology*, **17** (3), 687–691.

155. Popovici, M., Gich, M., Niznansky, D., Roig, A., Savii, C., Casas, L., Molins, E., Zaveta, K., Enache, C., Sort, J., de Brion, S., Chouteau, G., and Nogués, J. (2004) Optimized Synthesis of the Elusive ε-Fe_2O_3 Phase via Sol - Gel Chemistry. *Chem. Mater.*, (17), 5542–5548.

156. Morber, J.R., Ding, Y., Haluska, M.S., Li, Y., Liu, J.P., Wang, Z.L., and Snyder, R.L. (2006) PLD-assisted VLS growth of aligned ferrite nanorods, nanowires, and nanobelts-synthesis, and properties. *J. Phys. Chem. B*, **110** (43), 21672–21679.

157. Sakurai, S., Tomita, K., Hashimoto, K., Yashiro, H., and Ohkoshi, S.I. (2008) Preparation of the nanowire form of ε-Fe_2O_3 single crystal and a study of the formation process. *J. Phys. Chem. C*, **112** (51), 20212–20216.

158. Kelm, K., and Mader, W. (2005) Synthesis and Structural Analysis of ε-Fe_2O_3. *Zeitschrift für Anorg. und Allg. Chemie*, **631** (12), 2383–2389.

159. Sakurai, S., Shimoyama, J., Hashimoto, K., and Ohkoshi, S. (2008) Large coercive field in magnetic-field oriented ε-Fe_2O_3 nanorods. *Chem. Phys. Lett.*, **458** (4), 333–336.

160. Chai, G., Huang, W., Shi, Q., Zheng, S., and Wei, D. (2015) Preparation and characterization of lambda-Ti_3O_5 by carbothermal reduction. *J. Alloy. Compd.*, **621**, 404–410.

161. Bergerud, A., Buonsanti, R., Jordan-Sweet, J.L., and Milliron, D.J. (2013) Synthesis and Phase Stability of Metastable Bixbyite V_2O_3 Colloidal Nanocrystals. *Chem. Mater.*, **25** (15), 3172–3179.

162. Gich, M., Fina, I., Morelli, A., Sánchez, F., Alexe, M., Gàzquez, J., Fontcuberta, J., and Roig, A. (2014) Multiferroic iron oxide thin films at room temperature. *Adv. Mater.*, **26** (27), 4645–4652.

163. Bergerud, A., Selbach, S.M., and Milliron, D.J. (2016) Oxygen Incorporation and Release in Metastable Bixbyite V_2O_3 Nanocrystals. *ACS Nano*, **10** (6), 6147–6155.